NTNU – Trondheim
Norwegian University of
Science and Technology

Photoluminescence study of as-grown self-catalyzed GaAs/AlGaAs core-shell nanowires

Patrick Rene Tollefsen Slåttnes

Master of Science in Electronics
Submission date: June 2012
Supervisor: Helge Weman, IET
Co-supervisor: Phillip Olk, IET

Norwegian University of Science and Technology
Department of Electronics and Telecommunications

Abstract

A macro-photoluminescence study of self-catalyzed nanowires, using a specialized setup for this purpose, has been performed. Several samples were even compared to single nanowire micro-photoluminescence measurements, on the same samples, done by other students in the nanowire group at NTNU. The macro-photoluminescence measurements were done by changing parameters such as temperature and excitation power. A 532 nm laser was used to excite the wires and the photoluminescence was measured by a CCD detector attached to a spectroscope.

Using macro-photoluminescence measurements in a qualitative comparison with measurements done on single nanowires by micro-photoluminescence spectroscopy can give the researcher a decent understanding of the quality of the sample and its contributions to photoluminescence. Measurements done in this thesis show probable contributions from most types of transitions expected in zinc-blende nanowires, consisting of such defects as dense zinc-blende/wurtzite heterostructures, highly twinned regions, but also from nanowires of higher purity.

As nanowires move closer to the realization of e.g. nanowire based solar cells, such macro-photoluminescence measurements will become increasingly important in deciding the overall quality of the grown structures.

Sammendrag

Studie av makro-fotoluminescens av selv-katalyserte nanotråder, ved bruk av et spesialbygd eksperimentelt oppsett, har blitt gjennomført. Flere prøver ble til og med sammenlignet med mikro-fotoluminescens målinger gjort på samme type prøver, utført av andre studenter i Nanotråd-gruppen ved NTNU. Makro-fotoluminescens målingene ble utført ved å variere parametre som temperatur og eksitasjons-effekt. En 532 nm laser ble brukt til å eksitere nanotrådene og fotoluminescens ble målt av en CCD detektor koblet til et spektroskop.

Ved bruk av makro-fotoluminescens målinger i en kvalitativ sammenligning med målinger gjort på enkle nanotråder ved mikro-fotoluminescens spektroskopi, kan forskere få en betydelig forståelse av kvaliteten på prøven og de forskjellige bidragene til luminescens. Målinger gjort i denne masteroppgaven viser mulige bidrag fra de fleste typer defekter som er forventet å eksistere i zinc-blende nanotråder, bestående av defekter som tette lag av zinc-blende/wurtzite heterostrukturer, *twinned* områder, men også fra renere nanotråder uten defekter.

Etter hvert som realiseringer av nanotråd-baserte solceller nærmer seg, kan slike makro-fotoluminescens målinger bli et viktig redskap i bestemmelsen om den generelle kvaliteten på nanotråd-strukturene.

Acknowledgement

I would like to thank my supervisors, Prof. Helge Weman and Dr. Phillip Olk, for all their help during this project. Helge Weman's overall understanding on the concept of nanowires is astounding; a force keeping me motivated during the work on this project. I would also thank him for taking me as one of his students. Phillip Olk's patience, and understanding of optics, was highly valued in the months leading up to the final product.

I would also like to thank Lyubomir Ahtapodov and Terje Sund Mjåland for the fruitful discussions on the topic of nanowires, and for their measurements on single nanowires on some of the same samples as I studied.

Lastly I would like to thank Dong Chul Kim for patterning a sample just for me. And Abdul Mazid Munshi for growing said sample and for SEM images used in this thesis. The patterned sample was unfortunately not used in this work.

Contents

List of Figures

List of Tables

Abbreviations

As	Arsenide
Au	Gold
CBE	Chemical Beam Epitaxy
CVD	Chemical Vapor Deposition
EBL	Electron Beam Lithography
EM	Electromagnetic
FCC	Face Centered Cubic
Ga	Gallium
HCP	Hexagonal Close Packed
He	Helium
HVPE	Hydride Vapor Phase Epitaxy
LED	Light Emitting Diode
LHe	Liquid helium
MBE	Molecular Beam Epitaxy
MOCVD	Metalorganic Chemical Vapor Deposition
ND	Neutral Density
NIR	Near Infrared
NW	Nanowire
PL	Photoluminescence
Si	Silicon
VLS	Vapor-Liquid-Solid
WZ	Wurtzite
ZB	Zinc Blende

Introduction

The theoretical understanding of semiconductor nanowires, has grown considerably the last decades, and it still is. This knowledge is growing because of the expected boom in nanotechnology the coming years, and is spread across many different fields of science; theoretical quantum mechanical calculations, [1, 2], structure formation [3, 4], organic chemistry [5], optics [6, 7, 8], and even medical research and devices [9], to name a few.

Nanowires grown by molecular beam epitaxy, catalyzed by deposited metal droplets or self-catalyzed, have been thoroughly scrutinized in the scientific community thus far. This include several methods for characterization; e.g. temperature dependent optical studies, [10], polarization dependent optical studies and electrical characterization and structural characterization, [11]. Self-catalyzed nanowires, patterned and non-patterned, has gained momentum in nanowire research due to their possible integration with silicon-based technology.

This thesis is concentrating on the macro-photoluminescence, macro-PL, study of self-catalyzed nanowires grown at NTNU. These nanowires are all grown on p-doped Si(111) substrates. Both GaAs core and GaAs/AlGaAs core/shell nanowires will be studied using a specialized setup for macro-photoluminescence measurements using a spectroscope. This setup will be built as part of this thesis. A few nanowire samples will be compared to micro-photoluminescence measurements done by Lyubomir Ahtapodov and Terje Sund Mjåland. The goal is to qualitatively find out if macro-photoluminescence studies done on nanowire samples are a relevant method for future use.

1 Theory

1.1 A solid state

1.1.1 Nanowire growth

The science of NW growth may be one of the most important areas on the subject of NWs. Without complete control over growth, engineering promising technologies involving these small structures, e.g. NW transistors [12], would be very difficult.

Different mechanisms for NW growth exist. The most common one is the Vapor-Liquid-Solid mechanism (VLS). The mechanism was first proposed by Wagner and Ellis in 1964 for the explanation of silicon, (Si), whisker growth [13]. They understood the importance of a liquid alloy catalyst as part of the growth, as this droplet acted as a sink for the Si vapor introduced and possibly as the catalyst for the growth itself. The droplet became supersaturated with Si, which then proceeded to the liquid/solid interface and precipitated as part of the solid crystal. With sufficient time and continued introduction of Si-rich gas, a whisker was formed, with the catalyst droplet riding on top during growth, as seen in figure 1.1. They also understood that the same explanation could be applicable for several metals and other semiconductors, i.e. the same behavior during growth, and thus that a possible application of this growth-mechanism could be important in the future.

Other mechanisms for growth are also applicable, as mentioned above, e.g. vapor-solid or vapor-solid-solid growth, but the most important one by far is the VLS mechanism. All NWs studied in this thesis are grown by the VLS mechanism and performed by members of NTNU's Nanowire group responsible for growing samples, led by Bjørn-Ove Fimland. The other mechanisms will therefore not be described in this thesis.

Direct observation of the VLS mechanism by Wu and Yang [14], showed three distinct stages during growth:

1. Metal alloying
2. Crystal nucleation
3. Axial growth

Before the first step, gold (Au), or some other suitable metal, is deposited on to the sample. This can be achieved by several methods, one of them is to pattern the sample by lithographic methods, well known from e.g. the semiconductor industry, before depositing the metal. Thus the metal can be selectively patterned on the sample as small dots, with nanoscale dimensions, covering the surface and suitably dispersed. Using a growth chamber, a gas mixture is introduced into the system

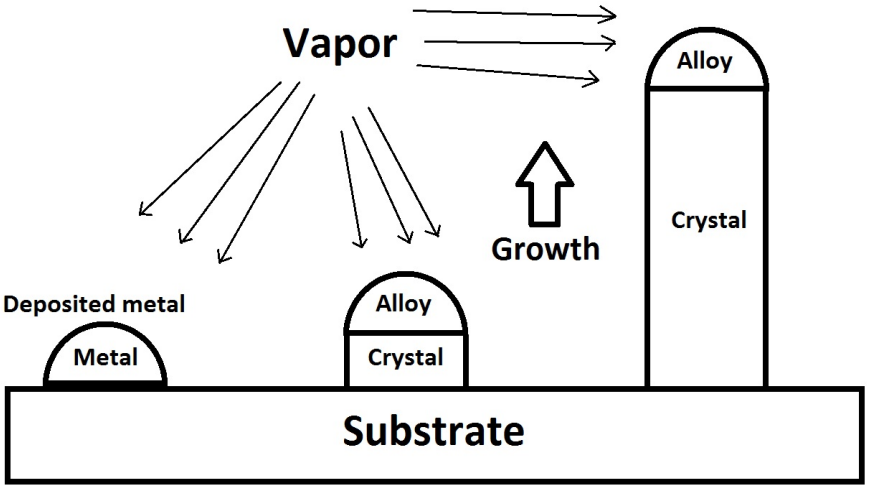

Figure 1.1: Above, a simple representation of VLS growth using metal seeds as catalyst can be seen, [13].

at a specific temperature and pressure for the metal in use and the crystal to be grown. The gas mixture introduced must contain the elements for crystal growth, e.g. gallium (Ga) and arsenide (As) rich gas for GaAs NWs. As the elements for crystal growth are in the vapor phase, they condense at the sample surface. This condensation will dilute the metal catalysts, even if they are solid, to form an alloy. This alloy will melt at the temperature in use, forming a droplet, because of the dissolution of the vapor Ga and As into the solid. This droplet will exist in parallel with a solid phase as long as the solid phase of the metal is less diluted than needed for liquefaction. Continued introduction of the gas mixture will lead to the droplets growing in size. Condensation of the vapor phase onto the droplets increase their saturation of Ga and As. Using phase diagrams of the alloy one can see how the droplets will cross into a region where both a liquid and crystal phase exist, as shown in the paper by Wu and Yang [14]. This means that nucleation has started. As the droplets reach supersaturated levels, crystal growth begins in the axial direction. As long as enough Ga and As are introduced in the vapor phase, the growth will continue. Stopping the growth can be achieved by stopping the introduction of crystal elements in the vapor phase, i.e. shutting off the supply of gas rich in Ga and As needed for growth.

Although VLS can explain the mechanism behind growth of several types of NWs, different methods can be used to initiate this mechanism. Chemical vapor deposition(CVD), is such a method. Other methods include metalorganic chemical vapour deposition (MOCVD), molecular beam epitaxy (MBE), chemical beam epitaxy (CBE), hydride vapour phase epitaxy (HVPE) and laser ablation, to name a few. As with the different growth mechanisms, each of the methods applicable for nanowire growth have their strengths and weaknesses. For III-V semiconductor nanowires, CVD may be the cheapest and easiest method to use, but the nanowires used in this project are grown using the MBE method.

MBE is a method well suited for deposition of GaAs, but also other materials. The reaction chamber is evacuated to an ultra high vacuum before deposition takes place. Reaction temperatures usually lie in the range 500 to 900 ^{o}C and the method allows for very precise control over deposition of layers with atomic resolution of thickness. In a GaAs growing scheme, solid Ga and As are usually heated in separate source cells, creating a stream of atoms striking the substrate to be processed. At the substrate surface the atoms react and contribute to the GaAs crystal formation. MBE is used to grow all NWs studied in this thesis, and the Nanowire group at NTNU has extensive experience using this method.

It is also possible to create NWs by using another form of catalyst than metal, as explained by Plissard et. al. [15]. They grew self-catalyzed NWs on a Si (111) substrate, using Ga droplets as the seed for growth. By using a substrate such as Si, the technology could be more easily transferred to the existing fabrication methods used in the industry and for easy integration with existing Si-based electronics. Si is also a fairly cheap material, especially when compared to e.g. GaAs. The Si substrate was first covered in SiO_2 before patterning. Small holes, serving as openings to the Si(111) surface and as traps for in situ formation of Ga droplets, were then processed through lithographic methods using EBL and etching. The Ga droplets were formed during a pre-deposition step, involving only Ga introduced into the chamber. Interestingly, the group also reported growth *without* intentionally forming Ga droplets as catalysts, although the NWs probably grew from droplets forming anyway in the patterned holes during introduction of Ga and As precursors. Note that the mechanism behind growth still is VLS, explained above.

As Wagner and Ellis predicted, NWs of today are constructed of different substances depending on the possible technological application they can be used for, or the scientific interest in question. For optoelectronic applications, direct bandgap semiconductors is important, e.g. GaAs or InP, and thus Si is of no use in the NW itself. GaAs and InP is binary compounds, but even ternary and quaternary compounds is important in such applications. If the application is as simple as a nano-sized conductor, the NWs may be constructed from metals such as e.g. Cu or Au. Even nano-sized insulators may be constructed with the use of insulating substances. Combining the possibility of using binary, ternary and quaternary compounds and the possibility of introducing heterojunctions represents almost overwhelming possibilities in future applications in many engineering fields.

1.1.2 Structure

Concentrating on semiconductor NWs, relevant information about their behavior comes from understanding the crystal structure, as is the case for all other semiconducting materials used in the engineering fields. In this thesis, GaAs nanowires are being studied, and thus it is relevant to look closer at this III-V binary semiconductor and the possibility of introducing heterojunctions into NWs.

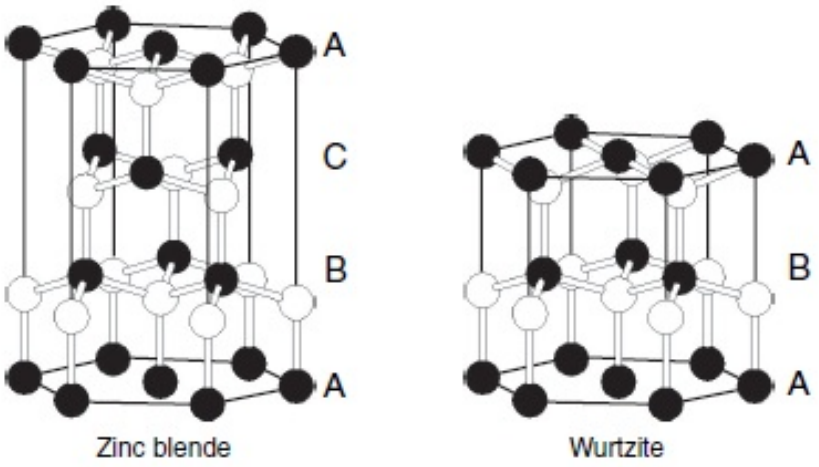

Figure 1.2: Two important crystal phases for GaAs are shown above; zinc-blende on the left and wurtzite on the right, [16].

Two crystal structures are important in the study of GaAs NWs: the wurtzite (WZ) and zinc-blende (ZB) crystal phases. These have several things in common. The WZ structure can be understood as two hexagonal close packed (HCP) structures interpenetrating, while the ZB structure can be understood as two face centered cubic (FCC) structures interpenetrating. Thus one can visualize both structures as composed of interpenetrating simpler structures. Both structures, of course, contain two types of atoms, Ga and As in our case, and they contain the same amount of atoms. For GaAs semiconductor bulk and thin films the crystal structure is of ZB with a reported lattice parameter of approximately a = 5.65 Å, [17]. Self-catalyzed GaAs NWs are also found to be primarily of ZB crystal phase, as reported by Bauer et. al. [18], with the possibility of WZ segments forming as defects as discussed in the next sub section. However, GaAs grown NWs by a metal catalyst almost always prefer the WZ phase, thoroughly investigated by Glas et. al. [3], with short segments of ZB phase stacked in between. Other methods exist to engineer the crystal phase into either ZB and WZ, e.g. by including Sb into the growth scheme as investigated by D. L. Dheeraj et. al. [11]. Thus, using a metal catalyst is not defining in the formation of the WZ phase, although it also plays its part. The lattice constants of GaAs WZ is approximately a = 4 Å, with c = 6.6 Å, given by the ratio of approximately c/a = 1.65. In the <111> direction of the ZB crystal phase the stacking of atoms can be described by the sequence

ABCABCABC... In the <0001> direction in the WZ crystal phase the stacking can be described as ABABAB... Figure 1.2 show a representation of these crystal phases.

Interestingly, in bulk form and at ambient pressures, GaAs never exhibits a WZ phase.

Short segments of ZB in a WZ NW are possible, the so called polytypism of ZB-WZ phases of many III-V semiconductors, and can be a big problem for engineering purposes, as one looses control over the behavior of the wires in e.g. optoelectronic applications. Sometimes, these short segments of the ZB phase is wanted, and can thus be included in a growth scheme. Such WZ GaAs wires, with ZB inserts, have been investigated in a paper by D. L. Dheeraj et. al. [19].

By the inclusion of wanted segments, one can engineer the energy bands of the NW, and thus the behavior under e.g. optoelectronic applications. The main difficulties however, are the unwanted inclusion of segments and faults, problems that would have to be controlled during growth.

1.1.3 Structural defects

The biggest obstacles during growth are the inclusion of impurities and formation of defects as e.g. stacking faults and unwanted changes in crystal phase. One can divide the defects in two classes; point defects and extended defects. Point defects occur at a single lattice site, while extended defects occur over a wider range. The inclusion of an impurity atom at interstitial lattice sites and the removal or replacement of basis atoms at the lattice sites by impurities are examples of such defects. Another point defect can be the swapping of atoms at lattice sites, e.g. a Ga atom and As atom swapping place, forming an irregularity in the crystal structure.

Extended defects include edge and screw dislocation, twinning and polytypism of the ZB-WZ phases: stacking faults and extended segments of unwanted crystal phase. A presentation of a selection of such extended defects can be seen in figures 1.3 and 1.4.

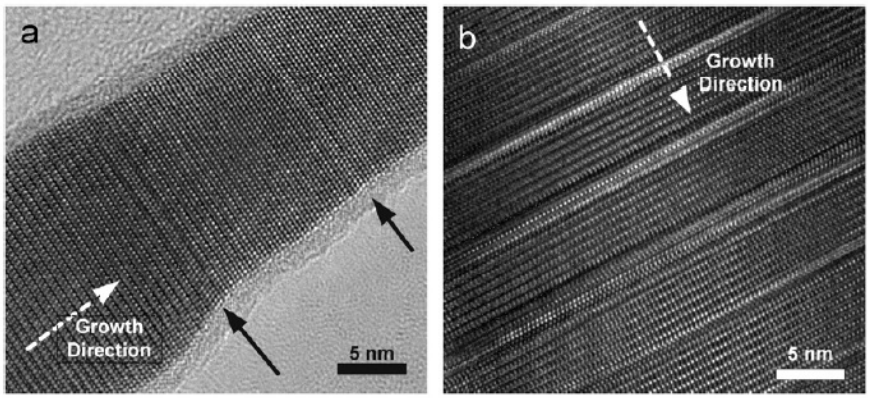

Figure 1.3: HR-TEM taken by Plante and LaPierre showing stacking faults in a WZ GaAs NW, also present in a periodic manner as seen in frame b, [20].

Stacking faults occur due to the free energy of the WZ and ZB phases being almost identical under certain conditions, as theoretically proven by several investigations [21, 22].

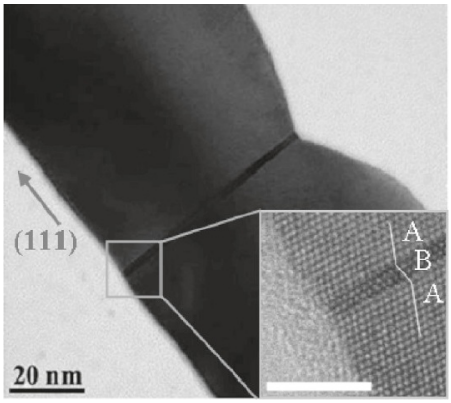

Figure 1.4: HR-TEM by Kang et. al. showing a thin twin defect in a pure ZB NW, [23].

Crystal twinning can be understood as a reflection of the stacking of planes at the twin interface, i.e. ABCABC**A**CBACBA, where the twin plane is shown in bold.

It is important to note that such defects can be found at different densities in e.g. a GaAs NW. These densities will affect the band alignment, and thus optical behavior of the NW, discussed further in the following sections.

1.1.4 Heterostructures and passivation layer

It is possible to include different materials into a NW, and thus engineer it even further. This is one of the strengths of NW technology. By introducing different precursors during the NW growth, a sudden change in the structure of the NW in the axial, and radial, direction is achievable. By doing this, the electronic band structure can be engineered even further. This *joining* of two, or more, different semiconductors is called heterostructures. Each of the different semiconductors has a different band structure, and when the two semiconductors join, the band structures of the two must align in some way, as will be explained in subsection 1.1.6.

Some of the NWs studied in this project have a second layer of material outside the core. Figure 1.1 does not show this layer. Imagine the exact same NW as shown in the figure, but with an added layer embedding the core, achieved through an added radial growth step at the end of the growing scheme. This is called a passivation layer, or a heterostructure, and is introduced for good reasons: this layer serves as a deactivation of surface states, which will, if unattended, lead to detrimental behavior of the core NW alone. These surface states will trap carriers and lead to more non-radiative behavior than without a passivation layer. Several studies have been performed on the issue of core/shell NWs, and on the improved optical properties, e.g. the study by Titova et. al. [24].

1.1.5 Electronic band structure

Before any interaction of NWs with their environment is discussed, an understanding on the concept of the electronic band structure, or the energy bands of solids, is needed.

In their quantum mechanical representation, electrons create a system of overlapping and interacting wave-functions because of the periodic structure of both semiconductors and quantum mechanical potentials. The crystal, with its atoms as the basis on the crystal lattice, creates a periodic potential felt by these fermions. Solving the Schrödinger equation for the electrons can be done by using different models. Each model presents, or could present, a slightly different picture of how the band structure is formed. Some models are best suited for different materials.

Using a simple model called the tight binding model, we understand the band structure as a consequence of the discrete energy spectrum of each atom. The tight binding model suggest that the atomic wave functions are rather tightly confined in real space. Also, the Pauli exclusion principle prevents any fermions from occupying the same quantum state, and thus such particles can not have the same principal quantum number n, i.e. energy, with the rest of the quantum numbers equal. Every atom has this property, i.e. atomic orbitals only accept a limited number of electrons, and the number of electrons in each orbital is dependent on the availability of unused sets of quantum numbers. The principal quantum number, n, represents the energy of the electron at the given orbital. The other quantum numbers are the angular momentum, l, the magnetic quantum number, m_l, and the spin projection quantum number, m_s. The rules assigning these quantum numbers their values decide how many electrons can be in the same orbital.

In a single atom, the combination of electronic states is quite simple, but as the atoms bind together to form the crystal it gets more complicated. The crystal atoms, bonded together, create the electronic band structure in semiconductors, a visualization of how allowed and forbidden bands form the landscape of energy vs wavevector of a solid. The forbidden bands are *areas* of energy which are not allowed to be occupied by e.g. electrons at given values of the wavevector. A similar explanation follows for the allowed bands, but of course here the particles and quasi-particles are allowed to exist. As mentioned above, the reason for these allowed and forbidden bands can be found in each atom, e.g. the forbidden area between the two first orbitals. We understand this as interference of the electronic wave functions found around the nucleus, giving constructive and destructive interference. The most simple visualization of the electronic band structure of e.g. GaAs can be presented by only looking at the top of the valence band and the bottom of the conduction band for all $\mathbf{k}$. These two simple bands are separated by a *bandgap* of certain value. No states can exist in this gap. However, using the Pauli exclusion principle, states near the band edges can be occupied, but only if they are available. No electrons with an equal set of quantum numbers can exist at the same place in a small volume. Depending on various factors that can change the quantum mechanical state of a fermion, e.g. a temperature increase, electrons can move between these available states.

Also, states can be introduced near the band edges, inside the forbidden gap. Such states are achieved by e.g. doping. Unwanted impurities can also introduce such states inside the gap.
In subsection 1.1.2, the ZB and WZ crystal structures were introduced. Using the explanation of the electronic band structure given above, one can understand why two different crystal structures would have two different band structures. Shown below are theoretical calculated band structures of ZB GaAs [25] and WZ GaAs [26]. Reported experimental values of the E_{gap} at the Γ point are approximately 1.52 eV for the ZB phase at 0 K and approximately 1.42 eV at 300 K [27]. A slightly higher value of approximately 1.47 eV is found for the WZ phase of GaAs [28] at 300 K, and very similar to the ZB band gap at 0 K, only differing in maybe tens of meV. However, there seems to be some controversy regarding the WZ band gap energy at 0 K, and the reported experimental values of these bandgaps vary some in the literature, but never far from the values given above. The same goes for theoretical values, but here the discrepancies are easier to understand since different theoretical models and/or parameter approximations often are used, e.g. lattice constants for the WZ and ZB crystal lattices.

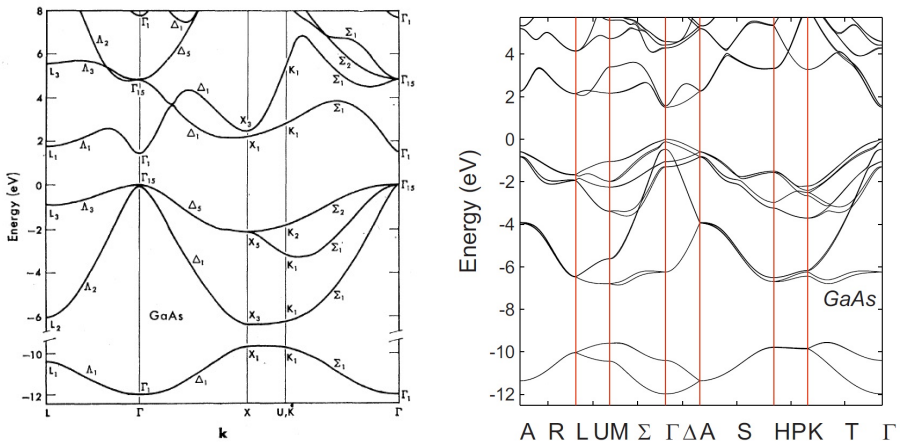

(a) (b)

Figure 1.5: Theoretical calculated band diagrams of the ZB and WZ crystal phase of GaAs. The ZB band diagram is shown in frame (a) and the WZ band diagram is shown in frame (b), [25] [26].

Looking at the band structure of GaAs something peculiar can be seen. The top of the valence band and the bottom of the conduction band are located at the same wavevector **k**. This means that a direct method of excitation is possible, i.e. an electron can easily be excited from the valence band to the conduction band at this **k** when a minimum of energy E_{gap} is involved in the process due to e.g. a photon. However, this is not the case for all semiconductors. Si has an indirect bandgap, which means that the top of the valence band and the bottom of the conduction band do not lie at the same wavevector. Thus, GaAs is much more suitable for optoelectronic applications, where photons excite electrons. The

process of exciting electrons is simply much more probable in a direct band gap semiconductor than an indirect one. For an indirect excitation by e.g. a photon of energy $E_\gamma > E_{gap}$, an exchange of momentum must also be performed, e.g. by phonons.

1.1.6 Band alignment

If heterostructures, introduced in subsection 1.1.4, are present in a NW it will affect the band structure and thus its optical and electrical properties. As the two different semiconductors are brought together, e.g. GaAs and AlGaAs, their bands must align. Here, Al is of course aluminium, and it is replacing some of the Ga atoms in the basis. The amount of Al introduced will decide how the semiconductor will behave, such as its optical behavior. E.g. when the molar fraction of Al in AlGaAs is over 0.45, the semiconductor will change its bandgap to an indirect one, making effects such as photoluminescence nearly impossible. The alignment of the band structure will classify what type of heterostructure it is. Primarily three types of alignment exist: type-I, -II and -III. Type-I alignment is straddled, type-II is staggered and type-III is broken, as can be seen from figure 1.6. In the case of interfaces such as GaAs/AlGaAs, were both can be found in the ZB crystal phase, very similar lattices leads to fairly good matching. This in turn leads to little dislocations and broken bonds, and an abrupt interface is possible. This abrupt transition is the basis for the alignment of the bands seen in figure 1.6.

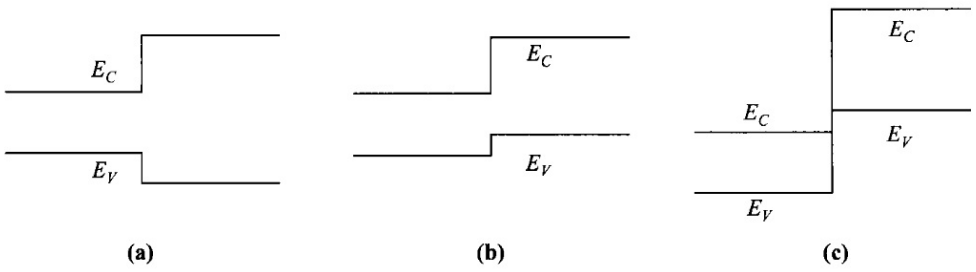

Figure 1.6: Three types of band alignment are shown above. From left to right: (a) straddled type-I, (b) staggered type-II and (c) broken type-III band alignments, [29].

An introduced shell such as AlGaAs, with its higher bandgap than the pure GaAs core, will lead to a type-I band alignment, when no doping is considered. Thus, there is an energy difference between the conduction bands of each semiconductor, and of course also the valence bands. However, this difference is not constant, and they do not need to be the same. These band *offsets* is of paramount importance when analyzing transitions from the conduction band to the valence band at the interface. For GaAs/AlGaAs heterointerfaces these offsets have been well documented and theorized.

In $Al_xGa_{1-x}As$, where x denotes the mole fraction of Al, reported values of the conduction and valence band offsets gives the relations shown in equation 1.1 and 1.2, [30];

$$\Delta E_c = (0.80 \pm 0.03)x \quad [eV] \tag{1.1}$$

$$\Delta E_v = (0.51 \pm 0.04)x \quad [eV] \tag{1.2}$$

Equation 1.1 are valid for $x < 0.45$, and 1.2 are valid for $0 \leq x \leq 1$. All AlGaAs shells grown on core/shell samples investigated in this thesis have $x \approx 0.3$. This gives us $\Delta E_c = 0.240 \pm 0.009$ eV and $\Delta E_v = 0.153 \pm 0.012$ eV. Thus $\Delta E_c / \Delta E_v = 60/40$, which fits well with a lot of work done in the field, as summarized by W. I. Wang, [31].

For temperature dependence, an $Al_xGa_{1-x}As$ passivation layer will have a bandgap at the Γ-point given by equation 1.3 and 1.4, in eV, where the temperature dependence of bandgaps by Varshni is used, [32].

$$E_\Gamma = E_\Gamma(0) - \frac{5.405 \cdot 10^{-4} T^2}{T + 204} \quad [eV] \tag{1.3}$$

where the bandgap energy at T = 0, $E_\Gamma(0)$, is given below with a molar Al content of x

$$E_\Gamma(0) = 1.519 + 1.155x + 0.37x^2 \quad [eV] \tag{1.4}$$

With an Al content of 0.3, the calculated value of the bandgap of an AlGaAs passivation layer would be approximately 1.899 eV at 10 K. This fits well using the calculated band offsets from equations 1.1 and 1.2, assuming a ZB GaAs low temperature bandgap of approximately 1.519 eV.

However, the band alignment between GaAs and AlGaAs can be changed quite dramatically by doping. Doping is the intended inclusions of impurity atoms, classified by their electronic contributions, i.e. electrons or holes. The impurity atoms can be either of n- or p-type, and are often called donors or acceptors respectively. The inclusion of donor impurity atoms, n-doping, leads to an abundance of electrons which can be excited at much lower energies. Acceptor impurity atoms, p-doping, leads to a scarcity of electrons, i.e. an abundance of holes. These donor and acceptor states are found close to the conduction and valence bands respectively, but inside the bandgap. Thus, the energy needed to excite a donor or acceptor is much smaller than the bandgap itself, and at even moderate temperatures, these carriers may thermalize into the conduction band or valence band, depending on the carrier type. At equilibrium, their Fermi levels will align. The

important point here is that these levels are changed when doping is introduced. Thus a different band alignment can be found for doped heterostructures.

Band alignment is also important for interfaces created when two different crystal phases are brought together. These may even be of the same material, such as GaAs. In fact, the band alignment between GaAs of ZB crystal phase and that of WZ crystal phase is very important to understand if a complete picture of GaAs optical and electrical properties is to be obtained. However, there is some controversy of what the bandgap of WZ GaAs is, and this will thus affect the detailed description of band offsets of the GaAs ZB/WZ interface. Theoretical values for GaAs WZ conduction and valence band offsets to their ZB counterparts have been performed and is given as $\Delta E_c = 0.117eV$ and $\Delta E_v = 0.084eV$, [33]. Thus the WZ/ZB interface represents a staggered type II band alignment, where the WZ conduction band is found 117 meV higher than the ZB conduction band, and the WZ valence band 84 meV higher than the ZB valence band.

1.2 Optical characteristics

In this project the main method of investigation is the relationship between the NWs themselves and light, i.e. photons, in spectroscopic setups. Thus a good understanding of how photons interact with the physical material is needed.

1.2.1 Photons vs excitons

Photons, which we denote γ, are the elemental particle representation of light. Electromagnetic radiation was first understood to be wavelike in nature, but experiments at the beginning of the 20th century needed another explanation for the nature of some phenomena seen. E.g. many experiments showed signs of the photoelectric effect, and it was Albert Einstein who introduced the light quanta, or photon, to explain these results. These particles contain both a wavelike and particle behavior, often considered as a so called wave-particle duality.

A photon carries energy calculated by the frequency, or speed and wavelength, as shown by equation 1.5

$$E_\gamma = h \cdot f = \frac{h \cdot c}{\lambda} \tag{1.5}$$

where E_γ is the photon energy, h the Planck constant, f the frequency, λ the wavelength of the EM radiation, and c the universal constant of the speed of light. The momentum of the photon is also important to know, given by equation 1.6

$$\mathbf{P}_\gamma = \hbar \cdot \mathbf{k} \tag{1.6}$$

where $\mathbf{P}_\gamma$ is the photon momentum, $\hbar$ is the reduced Planck constant and $\mathbf{k}$ the wave vector of the photon. $\hbar$ is simply given by $\hbar = h/2\pi$.

These two simple equations represent the most important behavior of a photon needed for explaining the interaction with solid matter. Photons hitting solid matter may interact in several ways; it can be reflected, absorbed or transmitted.

Depending on the photon energy, E_γ, and the semiconductor in question several things can happen when a photon hit a NW. Most importantly are the following cases;

If E_γ is less than the semiconductor band gap, $\mathrm{E}_\gamma < E_{gap}$, it will not excite any electrons enough for them to change orbitals. In other words the electrons can not gain enough energy to *jump* to a higher energy band, e.g. from the valence band to the conduction band at $\mathbf{k} = 0$ in GaAs. It may travel right through the solid, disregarding any other absorptive effects, as if the material is transparent, and we

observe that material as transparent to that frequency or wavelength of light.

On the other hand, if $E_\gamma > E_{gap}$, the photon may excite an electron enough to jump the forbidden gap. It may excite the electron such that it would be found around the conduction band edge, but it may also excite it much higher. Note that both energy and momentum must be conserved during such an event, as described by the conservation laws. This excitation can be observed by e.g. spectroscopic methods, as the excited electron falls back to its original energy band, a recombination of electron and hole. If the electron is found above the conduction band edge it may loose its energy in a non-radiative way, as to relax toward the conduction band edge before recombination. When an electron and a hole recombine, a release of energy is observed corresponding to the energy traversed, and a γ of exactly this energy is created. This is the main reason for photoluminescence in NWs at high temperatures.

However, at very low temperatures, a slightly different explanation is needed. When the γ hits the semiconductor NW with enough energy, the electron is excited and a bound electron-hole pair is formed. They are bound by the simple Coulomb force, and have zero net charge. This bound pair was first proposed in 1931 by Yakov Frenkel, a Soviet physicist, explaining the neutral excitation of matter by photons. The bound pair is called an exciton, an elementary quasi-particle of excitation. As long as the temperature is lower than the product k_bT, this type of excitation will dominate. These excitons exist at higher temperatures, but in much smaller numbers and are more difficult to see during a spectroscopic investigation. A recombination of the exciton will produce a photon of energy slightly less than the bandgap due to the binding energy of the electron and the hole when forming the exciton. Excitons themselves can be bound or they can be free to move in the crystal, but they are all unstable, in that they will ultimately recombine and loose energy to a photon or a phonon. Since electrons and holes have spins, the exciton will have a combination of these spins; they can be parallel with both the electron and the hole having their spins *up* or *down*, or they can be anti-parallel, with the electron and hole having their spins in opposite directions. Thus, excitons are bosons, and must fulfill Bose-Einstein statistics. The reason for the exciton being a boson can be found from its constituents as explained above. The binding energy of the free exciton in GaAs is approximately 4.2 meV, but properties such as this is highly dependent on NW size and geometry, and the type of exciton. In simple terms, one can say that exciton properties are due to only two factors; confinement in the nanostructure, such as a NW, and the Coulomb interaction between the electron and the hole forming the exciton.

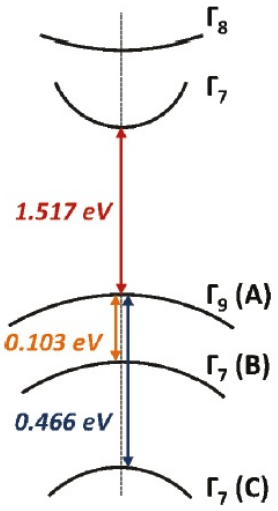

Figure 1.7: Energy of the free A, B and C excitons in WZ GaAs as shown by Ketterer et. al. [34]

The figure above show the energy of the free A, B and C excitons at the Γ-point for WZ GaAs, as reported by Ketterer et. al. by Raman spectroscopy [34].

Aside from Frenkel's exciton model, excitons can be divided into several types, depending on how they are formed and the material in question. The most interesting are listed below.

Frenkel excitons Small type, due to strong Coulomb interaction. In materials with a small dielectric constant.

Wannier-Mott excitons Usually in semiconductors due to larger dielectric constant. This means smaller Coulomb interaction, and larger exciton. Much lower binding energies than a Frenkel exciton.

Surface excitons Only living on the surface of a material. Electron in the vacuum, while hole is in the material.

Excitons resemble the ground state of a hydrogen atom because of the type of bond between the electron and the hole, i.e. Coulomb force. Thus we can model the exciton as having an energy very similar to a hydrogen atom, but we have to modify the function to take account of its constituents.

Using the effective masses of the electron and hole, using a reduced mass scheme, we can write

$$E_{\text{exc}} = -\frac{e^2}{4\pi\epsilon_0 r_1} \cdot \frac{1}{2n^2} \tag{1.7}$$

where r_1 is the radii of the state orbit, given by

$$r_1 = \frac{4\pi\epsilon_0\epsilon\hbar^2}{e^2\mu} \tag{1.8}$$

μ is the reduced effective mass of the exciton, given by

$$\mu = \frac{m_e^* m_h^*}{m_e^* + m_h^*} \tag{1.9}$$

where m_e^* and m_h^* are the effective masses of the electron and hole respectively. We see how the exciton depends on the dielectric constant. This is an important parameter defining materials, and thus explains why the excitons are so different in semiconductors compared to e.g. ionic crystals.

1.2.2 Excitation power dependence

During optical studies, a laser delivering light of a wavelength short enough for carrier excitation in semiconductors is mostly used. The experimenter often has the ability to vary the radiant flux, or radiant power, of the laser light, and it can be an important tool in the characterization of the observed reaction of the semiconductor, e.g. as in spectroscopic studies. The radiant power is indirectly a measure of the number of photons per unit time that are emitted from the laser, or more importantly, that are hitting a surface. The unit for radiant power is the watt, with dimensions joules/second. Thus, knowing the photon energy one can calculate the number of photons that e.g. interact with a surface per unit time. The radiant power is often varied by using filters in the experimental setup.

If clean, defect free semiconductors without any interfaces are being studied by varying the radiant power, one would not expect to see much differing optical behavior in e.g. photoluminescence spectroscopic studies. However, the observed PL intensity would surely be affected, as fewer photons would interact with the solid excitation power was decreased.

However, in real semiconductor objects, such as nanowires, defects of different types would surely be present, although at different densities depending on the quality of the structure and the material used. Heterostructures, discussed in subsections 1.1.4 and 1.1.6, can be an integral part of certain devices, but in many cases they are unwanted or unintended. Sandwiching two different materials together, e.g. in an AlGaAs/GaAs/AlGaAs stack or some other type of multilayer structure, using a very thin middle layer will create a potential well of a given depth and thickness. The depth is dependent on the materials used, and the well thickness is dependent on the thickness of the material being sandwiched. A very thin well may hold a very limited number of states at given energies, and we call it a quantum well.

Now, if such a quantum well is introduced in e.g. a NW, the observed PL from this quantum well alone is highly dependent on the laser power being used. With increasing laser power, there is a higher probability that higher energy states in the well are occupied, thus one fills the well with occupied states. Observed generated light from this well, where the higher occupied states recombine, will thus be blue-shifted as increased excitation power is used. Or, vice versa, red-shifted as decreased power is used. Thus, such shifting in observed spectra at changing excitation powers is important in knowing whether a peak in the spectrum can be attributed to quantum confined states. However, the well width also determines the lowest allowed energy state attainable.

1.2.3 Magnetic fields

Introducing a magnetic field to the NW, in whatever configuration, means that, formally, the Hamiltonian of the electron and hole needs to take this in effect. This also means that the exciton, being constructed from an electron and a hole, also should be affected by an applied external field. No detailed quantum mechanical calculations and approximations which could be used will be presented here. But a general overview is constructive.

First, before discussing the effects of a magnetic field on excitons, some general concepts regarding magnetic fields and matter must be introduced. Diamagnetism is an important effect observed in all materials, because all materials is built from atoms. Looking at it classically, electrons, orbiting the nucleus of an atom, create tiny current loops. These current loops create magnetic fields, and can be understood from classical electromagnetism and Ampère's law, i.e. that a closed loop of electric current will induce a magnetic field. When a magnetic field is applied to a material, the atoms tend to oppose the magnetic field. This can be understood as an effect derived from Lenz's law, i.e. that an induced magnetic field is created by the atoms to oppose the external magnetic field. However, for a complete understanding, a quantum mechanical derivation is needed. The effect is very weak, and some materials do not exhibit the evidence of such a field. The reason for this is simply that the effect is too weak compared to paramagnetic or ferromagnetic effects.

Important parameters when considering an applied external magnetic field are;

Cyclotron frequency Exposing electrons, and holes, to a magnetic field will lead to a motion described by the Lorentz force, given by equation 1.10.

$$\mathbf{F} = q[\mathbf{E} + (\mathbf{v} \times \mathbf{B})] \tag{1.10}$$

The electron, or hole, thus moves in a circle. The angular frequency is then given by the equation of cyclotron frequency, ω_c. The exciton also exhibit a motion, combining the relative motions of the electron and hole, and its cyclotron energy can be calculated, 1.11.

$$E_{cyc} = \hbar\omega_{cyc} = \hbar(eB/\mu) \tag{1.11}$$

where μ is the reduced mass of the exciton by the electron and the hole, defined by equation 1.9.

Magnetic field parameter A nondimensional parameter γ_B can be used to describe the field strength on exciton behavior. (Note here that γ_B is in no way connected to the photon symbol γ). If $\gamma_B \ll 1$, the weak field approximation can be used on the exciton Hamiltonian, i.e. first order perturbation theory.

If $\gamma_B \gg 1$ on the other hand, no such approximation can be used.

Equation 1.12 gives the value of γ_B

$$\gamma_B = \frac{\hbar e B}{2Ry^* \mu} \tag{1.12}$$

where Ry^* is the Rydberg energy of the exciton, given by equation 1.13.

$$Ry^* = \frac{\mu e^4}{2\hbar^2 \epsilon^2} \tag{1.13}$$

γ_B is used to find how comparable the applied magnetic field is to the Coulomb force binding the exciton. If the magnetic field strength is too high, the magnetic force felt by the electron and hole is larger than the Coulomb force, leading to deformation of the exciton.

Mainly two phenomena are interesting when looking at exciton recombination in spectroscopic magneto-PL studies; shift in observed PL and splitting of observed PL. Both are valuable tools in the investigation of nanostructures and can give information about the excitons and thus the structure itself. Only diamagnetic shift will be discussed here.

Diamagnetic shifts of exciton PL energy are often observed when varying the applied magnetic field during spectroscopic measurements in semiconductor nanostructures. It can be understood as a change in the relative motion of the electron and hole due to the Lorentz force from equation 1.10, thus changing the energy of the exciton. Different theoretical models exist for the exciton behavior in magnetic fields. In this experiment, fields possibly up to 11 T will be applied, and a first order perturbation on the Hamiltonian can be used. Equation 1.14 gives the diamagnetic energy-shift as a first order perturbation, by Taguchi et. al. [35]:

$$\Delta E = \frac{4\pi^2 \hbar^4 \epsilon_0^2 \epsilon^2 B^2}{e^2 \mu^3} \tag{1.14}$$

Finally, equation 1.15 gives us the exciton binding energy

$$E_b = \frac{\mu \cdot 13.6eV}{\epsilon^2} \tag{1.15}$$

which is only dependent on the reduced mass, μ, of the exciton and material dielectric constant, ϵ.

2 Method

There exist a variety of different methods to gain knowledge about semiconductor NWs. From structural investigations involving the use of e.g. TEM/SEM or diffraction, to optical and electrical investigations involving the use of laser excitation, spectroscopy and direct electrical measurements.

This project concentrated on the optical behavior of GaAs NWs, and thus spectroscopy was a natural method to use in such an experiment. However, there are different factors involved which can change the optical behavior of NWs, e.g. temperature, laser power, laser wavelength and magnetic fields. In this thesis, temperature variations and excitation power were the main variables involved in the measurements. An experimental setup was put together by the author, specially suited for macro-PL measurements.

A second cryostat, with equipment suitable for this setup, was ordered early spring 2012. This was supposed to be a setup particularly suitable for microphotoluminescence, μ-PL, measurements on single NWs. Unfortunately it was delivered too late for proper mantling and use before the thesis deadline and it will not be included here. A short discussion about this new setup is found in chapter 5.

2.1 Description of the experimental setup

The experimental setup consist of several parts, and is not necessarily limited to be used only in macro-PL measurements. The parts include the following:

- closed cycle cryostat with its own compressor, temperature controller and turbomolecular vacuum pump for evacuation of the cryostat
- spectrograph coupled with a CCD camera
- computer with suitable software for data capture
- optical equipment such as lenses, mirrors, filters, laser and dichroic mirror
- optical table serving as the frame of the total setup

2.1.1 The closed cycle cryostat

The cryostat is a CCS-100/CH-204N delivered by Janis Research Company. The cold finger and compressor are manufactured by Sumitomo Heavy Industries. The cryostat is the largest piece of hardware in the experimental setup, together with its connected components. In detail, it consists of valves and ports for evacuation, electrical connections and gas lines, a removable vacuum shroud and radiation shield, a sample holder and sample mount connected to the cryostat vacuum jacket

and cold head. It is used to isolate and cool the sample to be investigated to very low temperatures. To do this the chamber containing the sample is first evacuated to a very low pressure using the connected turbomolecular vacuum pump, ensuring that no condensation and ice forms on the sample or the inside of the chamber. When a satisfactory vacuum is achieved, $< 10^{-5}$ mbar, a compressor is turned on, the Sumitomo HC-4A Zephyr, starting the cooling sequence of the cryostat. Two tubes are connected between the compressor and the cryostat, each containing helium, He, in its gaseous phase. One tube contains warmer He gas to be returned to the compressor to be compressed, and thus cooled. This cooled He is then transported via the other tube from the compressor to the cryostat again, where it expands and chills the cryostat, forming a closed cycle. This design principle is the basis for the name of this particular type of cryostat, and it is thus called a closed cycle cryostat. A simple sketch of this cryostat connected to the compressor and turbomolecular vacuum pump is shown in figure 2.1.

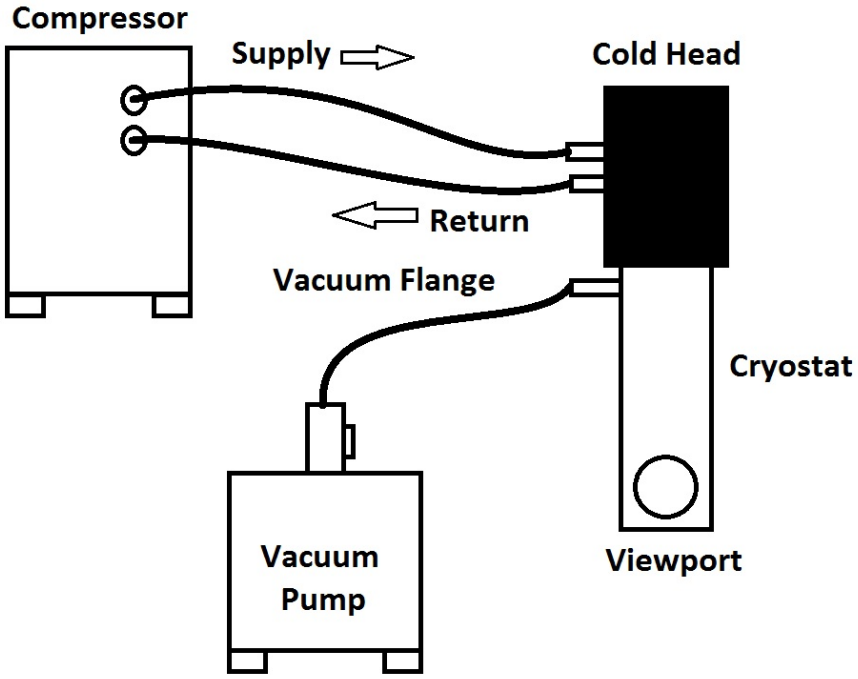

Figure 2.1: A simple sketch of the cryostat with its connected equipment, the compressor and the turbomolecular vacuum pump. Note that the compressor actually is placed in a different room than the cryostat and vacuum pump, due to it heat generating properties.

Since He is a commodity, and fairly pricey, this is an elegant solution to the problem. No He refilling is needed during operation, although it may need to be refueled at a later time after much use because of e.g. slow leakage of gas through the tube couplings. Actually, the expenses of operating such a cryostat is mainly from the compressor's high power requirements; it can chew off somewhere between 2 to 3 kW on average when it is turned on. It is also fairly noisy and generates a lot of

heat, and should thus be placed in another room than the cryostat, with adequate measures for cooling the surrounding air. It is important to note that the compressor may have degraded efficiency when no cooling solution of the surrounding air is installed, e.g. such as an air conditioner, ultimately leading to worse cooling performance in the sample chamber. It is also important to note that since the cryostat is of a closed cycle type using He gas instead of liquid He, the lowest possible temperature achievable on the sample is a few degrees above 4.2 K. Some closed cycle cryostats actually have the ability to cool the sample well below 4.2 K, utilizing smart solutions in the cryostat itself, helium-3 and more powerful compressors.

This closed cycle cryostat has some of these solutions installed, compactly known as the cryostat cold head, and is a large part of the cryostat itself. The compression and expansion of helium gas mentioned above is based on the Gifford-McMahon thermodynamic cycle. Compressed helium gas from the compressor is delivered to the cryostat cold head by the supply line. This high-pressure gas is fed to an inlet directly on a rotating valve disc, driven by a valve motor at the top of the cold head. As the valve disc rotates, an opening to the first cooling stage appear, and the high pressure helium gas is let through. The valve disc continues to rotate, closing the inlet opening. An expansion space is created as the compressed gas flows down through the first and second stage. Before the valve disc completes its first revolution, it uncovers an exhaust opening, leading to the return line connected to the compressor, and the high-pressure helium gas is free to expand and cool the stages. The complete revolution of the valve disc ends in closure of the exhaust port and now slightly colder stages. The temperature in the two cold stages are progressively decreased by the revolution of the valve disc and continued supply of compressed helium gas. The electricity needed for the valve motor is fed from the compressor directly by an electrical cable between the compressor and the cold head. This is somewhat a simplified explanation, as the cold head also consists of a moving displacer, slack cap and at least one surge volume, all driven by the pressure of the gas. But the explanation above holds nonetheless.

Before measurements can begin a sample needs to be loaded. In this experimental setup the vacuum shroud is bolted with screws to a plate adapter, which in turn is bolted to the optical table. The cryostat may actually be placed in any direction, but for easy mounting of the used optics it was decided to have the window openings at the cryostat as close to the table as possible. Because of this, an electrical operated crane was made by the workshop at the electronics building at NTNU. This was a custom solution for lifting the whole cryostat, except the vacuum shroud, when changing samples. Before lifting the cryostat, the clamp between the vacuum shroud and the cold head is removed. Ensuring that no vacuum is present in the shroud by opening the evacuation valve, the crane controls can be used to reveal the sample stage for sample loading.

2.1.2 The optical components

Several optical components were installed on the optical table for this experimental setup. Figure 2.2 shows the experimental setup, except the compressor and vacuum pump. We start with the laser and follow the light propagating through the setup.

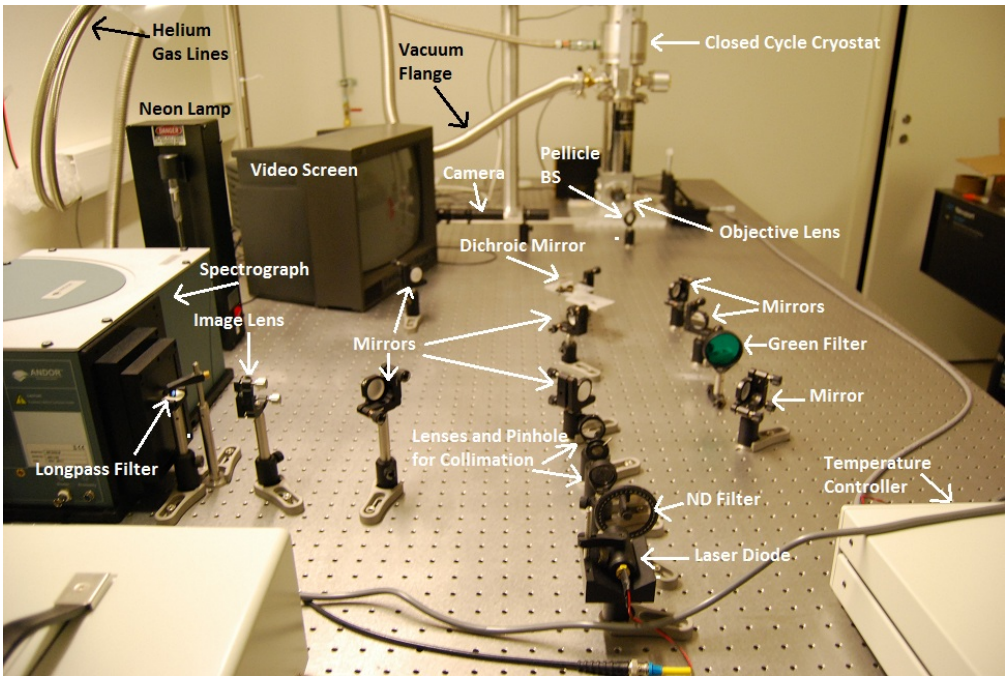

Figure 2.2: Photograph of the experimental setup with named components.

The laser used is a green laser diode, the same type found in the simplest of laser pointers. It is set to output a maximum of 4 mW, although it is rated at 5 mW. The wavelength is 532 nm, i.e. photon energy of 2.333 eV, enough to excite the NWs under investigation. Following the laser diode is a neutral density, ND, filter for varying the excitation power. This is manually controlled by turning the graded filter itself, as it is mounted as a wheel on an optical post. Two lenses, with a pinhole in between, are placed after the ND filter. This is used to collimate the laser as much as possible before it propagates further into the setup. It can also be used to adapt the beam width if wanted.

Several mirrors and a green filter are placed at the middle of the setup. The green filter ensures that only light of 532 nm can propagate further, as residual pump light from the diode laser may be present and show on spectra recorded during experiments. The mirrors is used to control the beam height and direction. One negative aspect of the green filter used in this setup is a loss of power; approximately 50 % of the power from the laser diode is lost in this filter. A dichroic mirror is used to separate the incoming light from the generated photoluminescence signal.

At the cryostat an objective lens is used to focus the laser light coming into the

cryostat, but also to gather the generated PL. The PL is then transmitted through the dichroic mirror on to a couple of mirrors used to raise the beam height to the input slit height at the spectrograph. A image lens is placed at the input slit of the spectrograph together with a longpass optical filter, so that only the PL is transmitted and no laser light. This describes the optical components used in this experimental setup. Optionally a video camera is available with its own set of optics. It is particularly useful when the focused spot size is in question or when looking at samples that have a certain structure, e.g. patterned NWs. Details on as-grown, non-patterned, NW samples are impossible to see using this camera, as these samples are very effective in trapping visible light, thus appearing as completely dark images. If the experimenter chooses to use the camera, a pellicle beamsplitter , BS, is used in front of the objective lens. Thus it is possible to excite the sample and view the laser spot at the same time. A white light emitting diode, LED, can be used in front of this pellicle BS, looking into the cryostat, if structured samples is to be viewed on the video screen.

From the image in figure 2.2 it may be difficult to see exactly what happens from the laser diode to the sample and back to the spectrograph. A sketch of the experimental setup shown in figure 2.3 is thus presented.

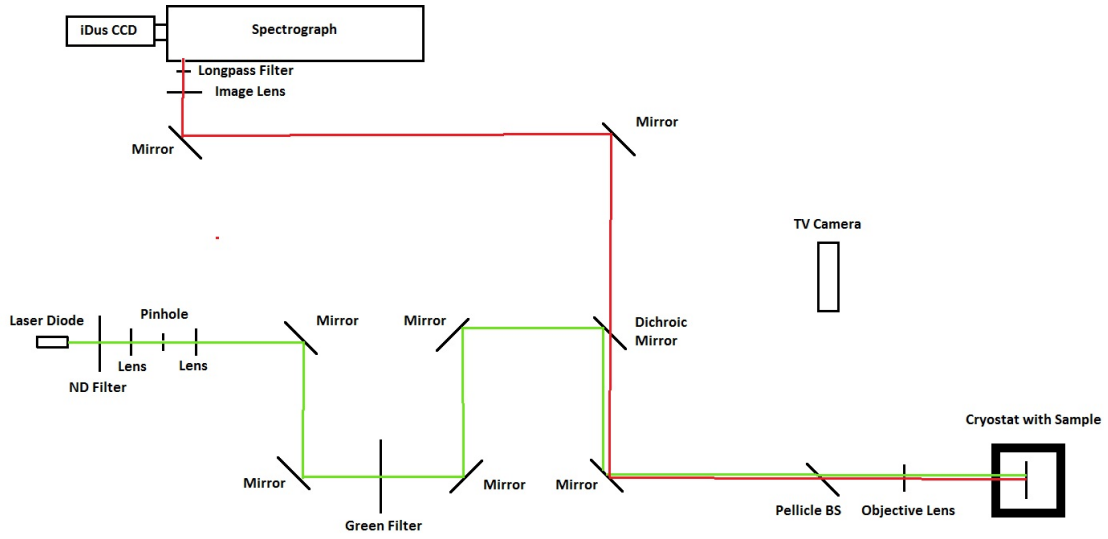

Figure 2.3: A simplified sketch of the complete experimental setup used in this thesis is shown above. 532 nm laser light is shown as green, while the generated photoluminescence is shown in red.

2.1.3 The spectrograph and temperature controller

The spectrograph used is an Andor Shamrock 303 Imaging Spectrograph and comes with an Andor iDus 401 CCD camera attached, a camera that is specially suitable for looking at NIR wavelengths. The spectrograph is of the widely used Czerny-Turner design; a very reliable setup and quite easy to understand from an operating standpoint. It comes with three different gratings; a 150 grooves/mm grating blazed at 800 nm and two 600 grooves/mm gratings, one blazed at 500 nm and the other at 1000 nm. Using the gratings with higher amount of grooves/mm will give a higher spectral resolution at the CCD chip, but intensity is lost since the light is spread over a wider area. The iDus CCD chip is chilled by a thermoelectric cooler, which in turn is ventilated by cooling fans. This setup provides CCD chip temperatures down to $-70\,^{\circ}\mathrm{C}$, but there is a possibility of connecting pipes for water cooling on the camera as well, leading to more effective cooling and chip temperatures down to $-100\,^{\circ}\mathrm{C}$. These low temperatures ensure good signal to noise ratio at the chip itself. A standard desktop computer is used together with the spectrograph and CCD camera via two USB cables. A software developed by Andor is then used during operation to control the spectrograph and the camera, e.g. the input slit opening, camera exposure and the grating to be used. Data is captured and saved on the computer hard drive for later use.

The temperature controller is a LakeShore Model 331, attached to the cryostat with a input/output connector, and can thus be used to control the temperature at the sample. It accomplishes this by heating a resistive element very close to the sample mount in the sample chamber itself. This heating is controlled through a negative feedback loop, where sensor-data from a thermometer close to the sample stage is fed back to the controller so that suitable parameters may be adjusted, e.g. the amount of current to be used in the resistive element. The feedback control loop is of a proportional-integral-derivative type, PID, with default parameter values. The operator may simply change the wanted stable temperature at the controller input, and the controller will do the rest of the job. However, a choice must be made when running the temperature controller at certain temperature ranges. Three levels exist, each with its own output range of heating power; low, medium and high. At low temperatures, e.g. when the operator wants a stable temperature of 10 K at the sample, low or medium ranges should be chosen. This ensures that the controller behaves correctly. If one chooses the high setting at such low temperatures, the sample temperature will swing widely around 10 K, with amplitudes observed as high as 3 K. The operator may also change specific parameters when needed, i.e. each of the feedback control variables; proportional, integral and derivative values. This specific temperature controller was stable enough at 10 K and ever more stable at higher temperatures. But below 10 K it had some problems keeping it at a stable value, e.g. at 7 K it would swing between 6 K and 8 K. The lowest possible temperature achievable is approximately 6 K. Temperature errors observed during measurements are listed in section 2.3.

Important information and details about this experimental setup for macro-PL measurements are listed below.

Table 2.1: Important parameters and details on the complete experimental setup used in this thesis.

Spectrograph	Andor Shamrock 303 Imaging Spectrograph
Spectrograph Grating 1	150 grooves/mm blazed @ 800 nm
Spectrograph Grating 2	600 grooves/mm blazed @ 500 nm
Spectrograph Grating 3	600 grooves/mm blazed @ 1000 nm
Spectrograph Camera	Andor iDus 401
Camera Pixel Size	26 μm x 26 μm
Camera Active Pixels	1024 x 127
Camera Maximum Cooling	$-100\,^{\circ}$C
Used Camera Cooling	$-50\,^{\circ}$C
Laser	532 nm laser diode
Laser Wavelength	532 nm
Laser Photon Energy	2.333 eV
Laser Spot Size	30-40 μm
Laser power density at 1 mW	450-250 W/cm^2
Cryostat	Janis CCS-100/CH-204N
Temperature Controller	LakeShore Model 331
Compressor	Sumitomo HC-4A Zephyr
Vacuum Pump	TP-75-DR (Oil free)
Vacuum Achievable	1 x 10^6 mbar
Power Meter	Thorlabs PM100 - S120B
Imaging Lens	LA4380
Imaging Lens, Focal Length	100 mm
Objective Lens	LA4725
Objective Lens, Focal Length	75 mm

2.2 The nanowires

The NW samples studied in this thesis are all of a self-catalyzed type, both core/shell GaAs/AlGaAs and bare GaAs core NWs. Two samples were even doped. Some of these samples were also studied by Lyubomir Ahtapodov and Terje Sund Mjåland, but with the NWs dispersed randomly on a Si_3N_4 grid on a Si substrate after breaking them off from the as-grown samples. This was done in order to do measurements on single NWs, i.e. μ-PL. These two types of measurements, macro-PL and μ-PL, on the same type of NWs could then be compared to see differing behavior, if such existed. The NWs in this thesis are supposed to be of pure ZB crystal phase, although defects in different forms were expected. Table 2.2 summarizes the details about the samples being measured.

Table 2.2: Table of important NW sample parameters.

	SC-88	SC-109	SC-139	SC-151	SC-153
Growth Chamber	MBE	MBE	MBE	MBE	MBE
Catalyst	Ga	Ga	Ga	Ga	Ga
Core/Shell	Core	Core/Shell	Core	Core	Core/Shell
Al_xGa_{1-x}, x	N/A	0.3	No	No	0.33
Dopants	N/A	N/A	N/A	Be	Be/Si
Doping concentration, [cm^{-3}]	N/A	N/A	N/A	$3 \cdot 10^{18}$	$3 \cdot 10^{18}/1 \cdot 10^{18}$
Growth temperature [^{o}C]	620	640/640	580	640	540/540

Nanowire sample SC-138 were not measured by the macro-PL experimental setup used in this thesis, but its μ-PL was measured by Lyubomir Ahtapodov and Terje Sund Mjåland. It was originally thought that both macro- and μ-PL measurements were done on SC-139. A misunderstanding between the experimentalists led to different samples being measured. However, μ-PL measurements done on SC-138 are still worthwhile to discuss because of a similar growth scheme as for SC-109, but with an added AlGaAs growth in the axial direction before Ga-droplet solidification. Also, macro-PL measurements done on SC-139 will be presented in the next chapter for completeness.

The NW sample growers are a group within the Nanowire research group here at NTNU. They are responsible for growing all the samples used in this thesis. All samples were grown on p-doped Si(111) substrates, treated with an acidic solution with an HF concentration of 5 %. The sample substrates were placed in the solution for approximately the same time, 2 seconds, but small deviations from this are possible. The important point is that such treatment will remove native oxide present, thus leading to much more homogeneous morphology after growth. Without this treatment, a lot of tilted NWs would be present on the as-grown samples. Apart from growing the samples, the growers also take SEM images. This is particularly useful in this thesis when measuring on as-grown samples, i.e. macro-photoluminescence study using spectroscopy. Using the SEM images from each as-grown sample, it is possible to estimate the number of NWs contributing to the observed PL. Using the approximate size of the laser spot hitting the samples and counting NWs on each sample to find the density, this amount can be estimated. The SEM images for each sample investigated using macro-PL methods are presented in appendix A.1.

2.3 The measurements

Measurements were done with a sample temperature beginning at 10 K and then at several higher temperatures. These values were chosen so as to have a decent spacing between each measurement. At each temperature the excitation power was varied using a ND filter. The measurements on each sample was concluded when no PL was detected due to e.g. too high temperature or too low excitation power. Also, when no signal was detected at a certain excitation power, this power was excluded in the next measurements at higher temperatures. E.g. if a signal was observed at 10 K at 1 μW excitation power, but not at 50 K, the 1 μW excitation power was omitted from measurements at 50 K and higher temperatures. Tables with details about the macro-PL measurements done on the different samples are found in appendix A.2.

All PL measurements have been fitted with one or several Voigt distributions, using the least squares method. The data was corrected on the wavelength axis, using a neon lamp and tabulated values from the NIST Atomic Spectra Database on the strongest chosen peaks. This deviation was then corrected for when doing the numerical analysis of the measured data. All plots were generated in Origin, a data analysis and graphing software from OriginLab. All numerical treatments of the measured data, e.g. spectroscope wavelength correction, were done in Matlab.

3 Results

Data taken from macro-PL measurements on several self-catalyzed NW samples is presented below. Most of the measured samples were qualitatively compared to μ-PL measurements on single NWs done by Lyubomir Ahtapodov and Terje Sund Mjåland. These are the same samples, but on different substrates, i.e. macro-PL measurements were done on as-grown samples, while μ-PL measurements were done on substrates with the same type of NWs dispersed on a Si_3N_4 grid. The exception is the comparison between macro-PL measurement from sample SC-109 and the μ-PL measurement from sample SC-138. It was first believed that μ-PL measurement were done on SC-139, but later investigations confirmed that it was done on SC-138. A comparison between macro-PL and μ-PL could thus not be done on SC-139. However, SC-138 was grown similar to SC-109, except with an added AlGaAs shell growth in the axial direction, performed before Ga-droplet solidification. The μ-PL measurements from SC-138 will thus be used in a comparison to both macro- and μ-PL from sample SC-109.

Data from SC-88 is presented first, followed by data from samples SC-109 and SC-138, SC-139, SC-151 and SC-153. Note that not all samples were successfully fitted using the Varshni equation. This will be discussed further in the next chapter.

3.1 Measurements from sample SC-88

First an overview of the measured macro-PL from sample SC-88 is shown in figures 3.1 and 3.2. The grating used is 600 grooves/mm, centered at 860 nm, with a 40 μm slit opening on the spectroscope. CCD exposure of 0.1 seconds at the highest excitation powers and 1 second at the three lowest was used at 10 K, while 1 second was used for both measurements at 110 K. μ-PL measurements done on SC-88 NWs were exceptionally bad, i.e. almost no detectable signal over background noise, and these were therefore not included here.

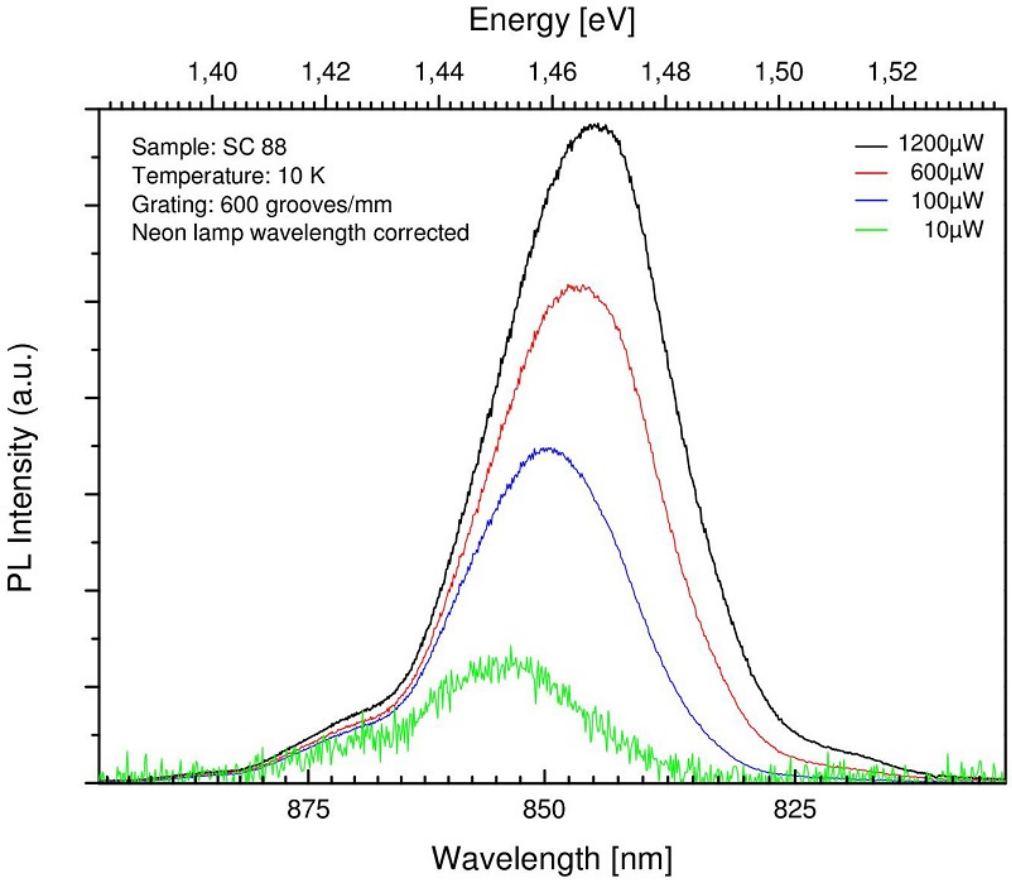

Figure 3.1: Peaks from macro-PL measurements done on of SC-88 at 10 K shown above.

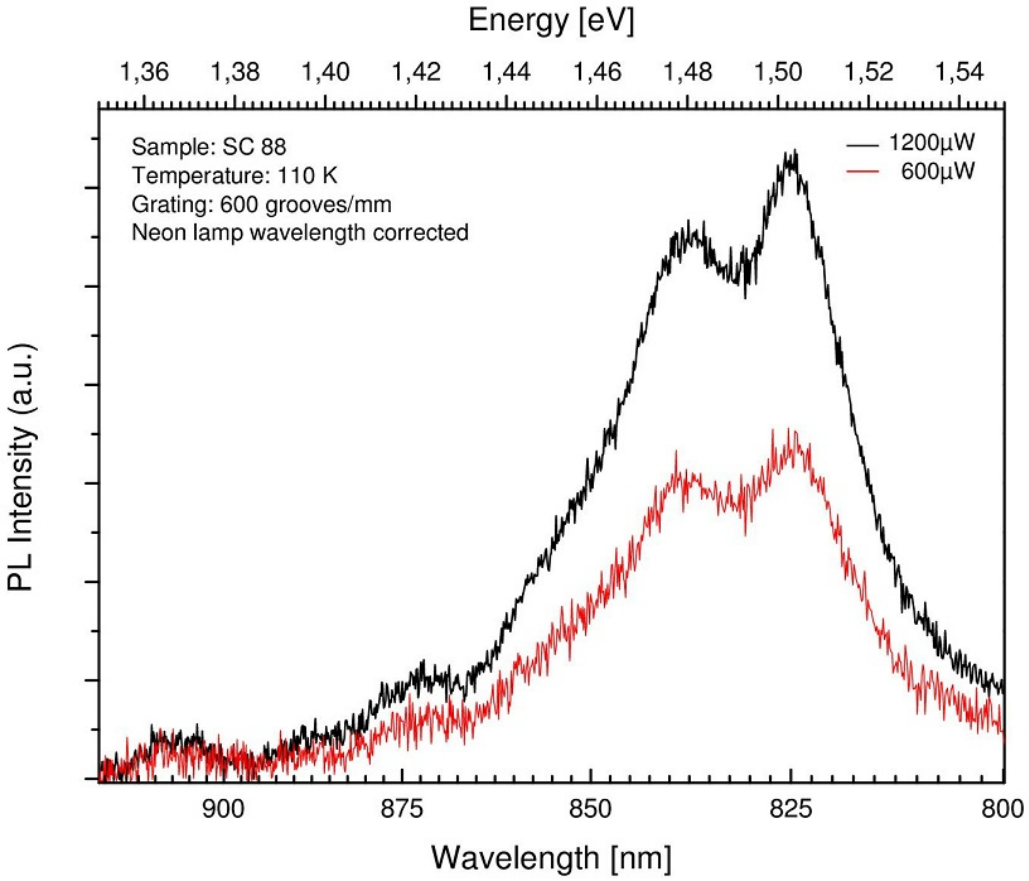

Figure 3.2: Peaks from macro-PL measurements done on SC-88 at 110 K are shown above. Note that measured PL intensity was low, thus high exposure was used. No PL was detected at or below 100 μW excitation power.

3.2 Measurements from samples SC-109 and SC-138

Overview of the measured macro-PL from sample SC-109 is shown in figures 3.3 and 3.4. The grating used is 600 grooves/mm, centered at 820 nm, with a 10 μm slit opening on the spectroscope, the lowest possible. CCD exposure of 0.01 seconds at all excitation powers was used at both 10 K and 280 K, except for 10 μW excitation power at 280 K. Here 0.5 seconds was used.

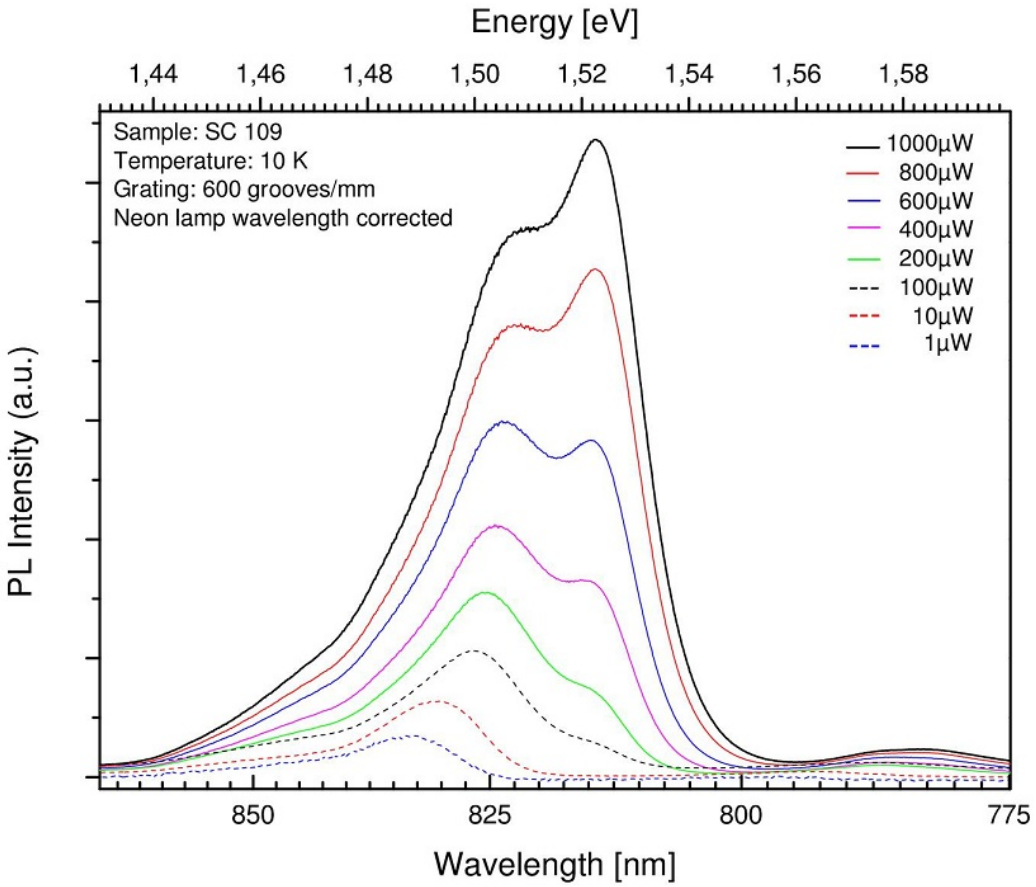

Figure 3.3: Peaks from macro-PL measurements done on SC-109 at 10 K are shown above.

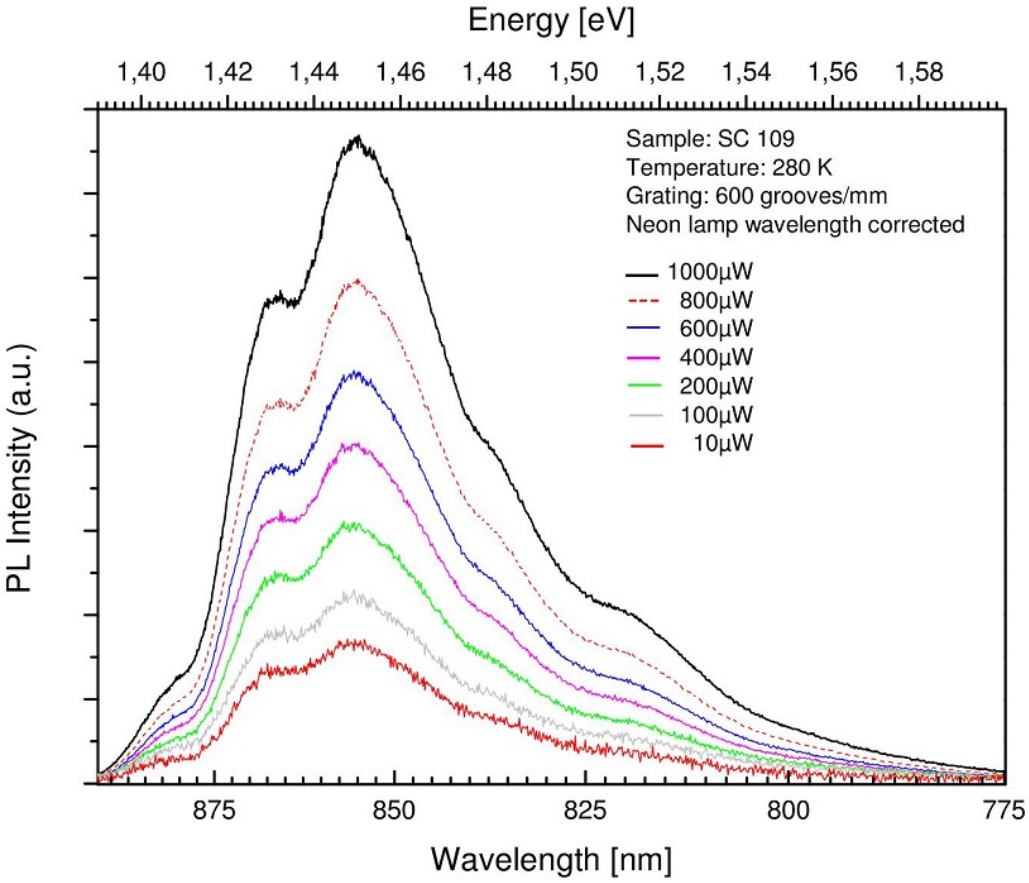

Figure 3.4: Peaks from macro-PL measurements done on SC-109 at 280 K are shown above. A very high PL intensity was observed for this sample, but no PL was detected with 1 μW excitation power used at 280 K.

Measurements on two single nanowires are presented in figure 3.5 and 3.6. Figure 3.5 presents data from nanowire NW2201 at 18 K, using excitation powers somewhat less than used on the macro-PL measurements shown in figures 3.3 and 3.4. Figure 3.6 shows measurements done on another nanowire, NW2211, at 24.6 K. The grating used in all the μ-PL measurements has 300 grooves/mm.
μ-PL measurements from sample SC-138 are presented in figure 3.7. This sample is very similar to SC-109, due to the same growth parameters used, except for an AlGaAs shell formation before Ga-droplet solidification. It was believed that macro-PL measurements were done on the same sample, but unfortunately a misunderstanding led to macro-PL measurements done on SC-139 instead, presented in the next section. However, μ-PL measurements done on sample SC-138 are of interest here due to its similarities to SC-109, as mentioned above.
Figure 3.8 shows the peak positions at given temperatures for SC 109. These peak positions were obtained from fitting the measured curves with one or several Voigt distributions, depending on the observable number of peaks. Only the strongest peak was then used in this figure. Error bars were first included at the peak positions, but they were so small that they were omitted. Highest error observed was in the 10^{-4} range. The scatter plot was then fitted with the Varshni equation

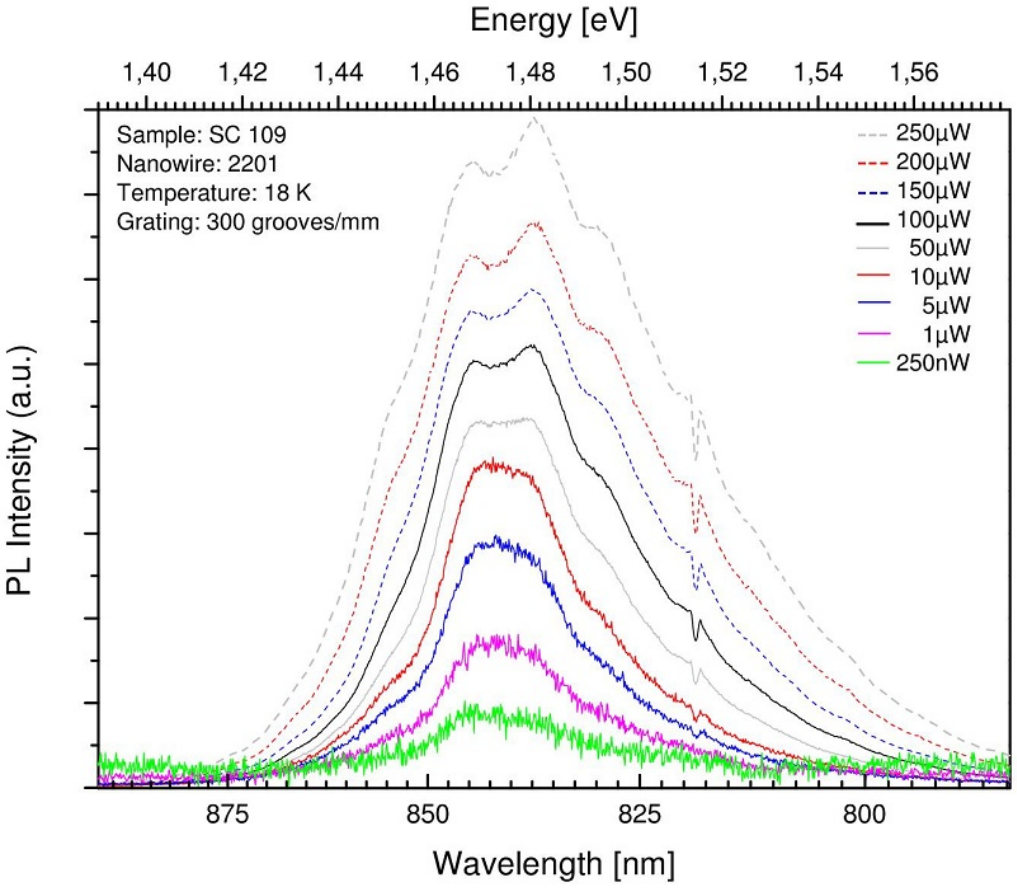

Figure 3.5: Measured μ-PL peaks from sample SC-109 done by Lyubomir Ahtapodov and Terje Sund Mjåland are shown above. The measurements were done at 18 K.

using the least mean squares method. Details of the fit is seen in the figure.

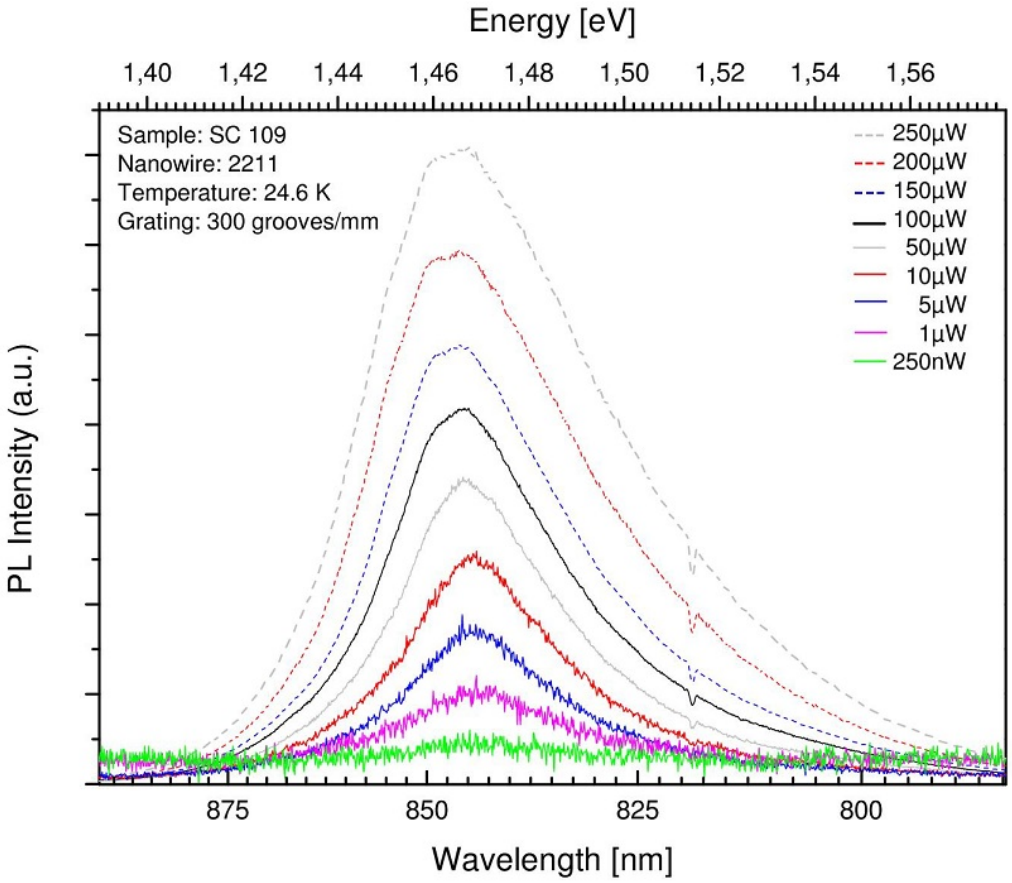

Figure 3.6: Measured μ-PL peaks from sample SC-109 done by Lyubomir Ahtapodov and Terje Sund Mjåland are shown above. The measurements were done at 24.6 K.

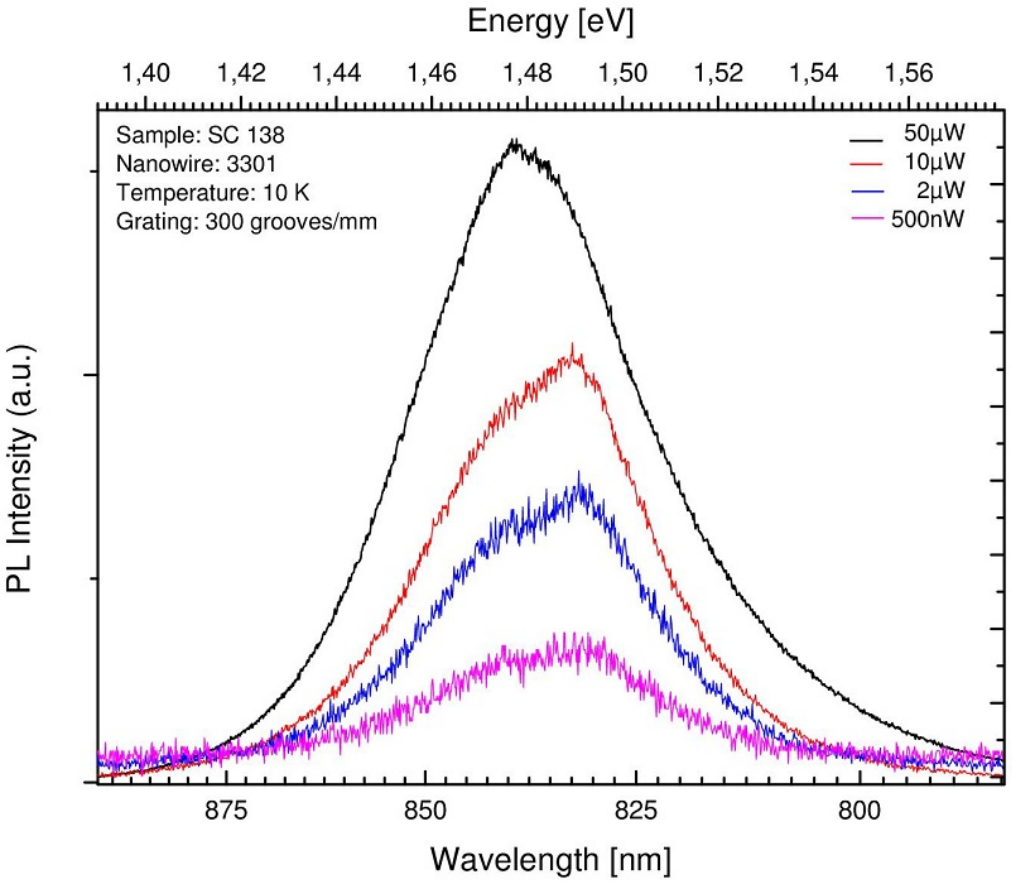

Figure 3.7: Measured μ-PL peaks from sample SC-138 done by Lyubomir Ahtapodov and Terje Sund Mjåland are shown above. The measurements were done at 10 K.

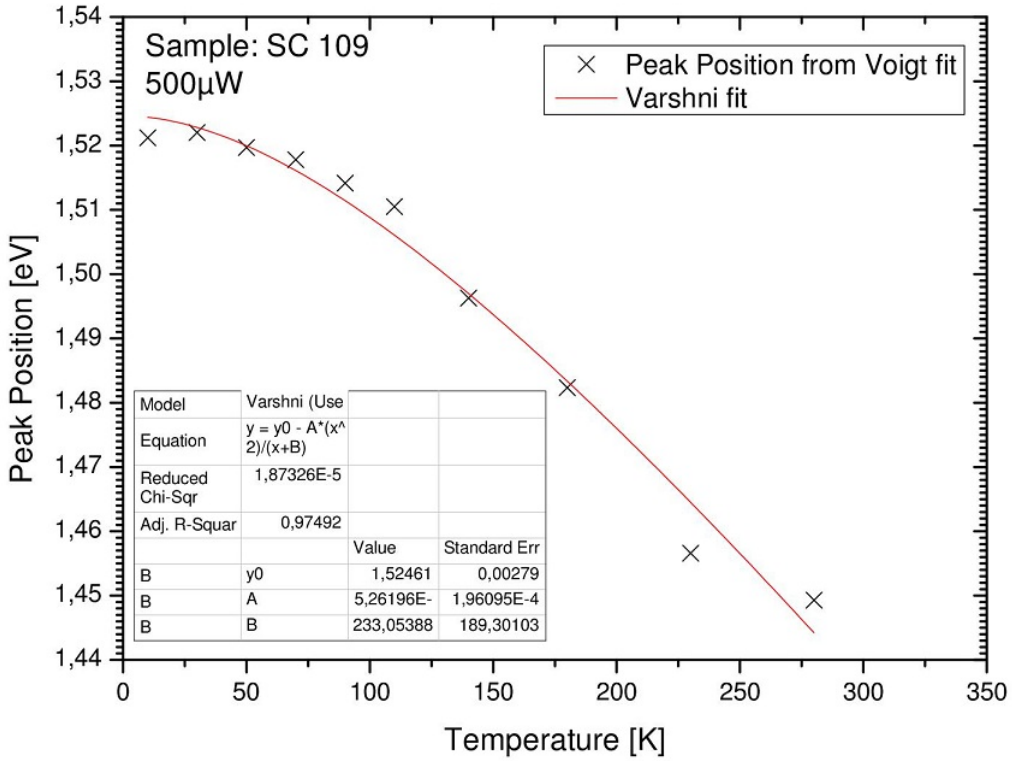

Figure 3.8: Scatter plot of the peak positions of the strongest peak different temperatures is shown above. Fitting was done using the Varshni equation in a least mean square sense. Details of the Varshni fit can be seen in the figure.

3.3 Measurements from sample SC-139

Overview of the measured macro-PL from sample SC-139 is shown in figures 3.9 and 3.10. The grating used is 600 grooves/mm, centered at 820 nm, with a 70 μm slit opening on the spectroscope. CCD exposure of 0.12 seconds at most excitation powers was used at 10 K, while 1 second was used for all excitation powers at 120 K.

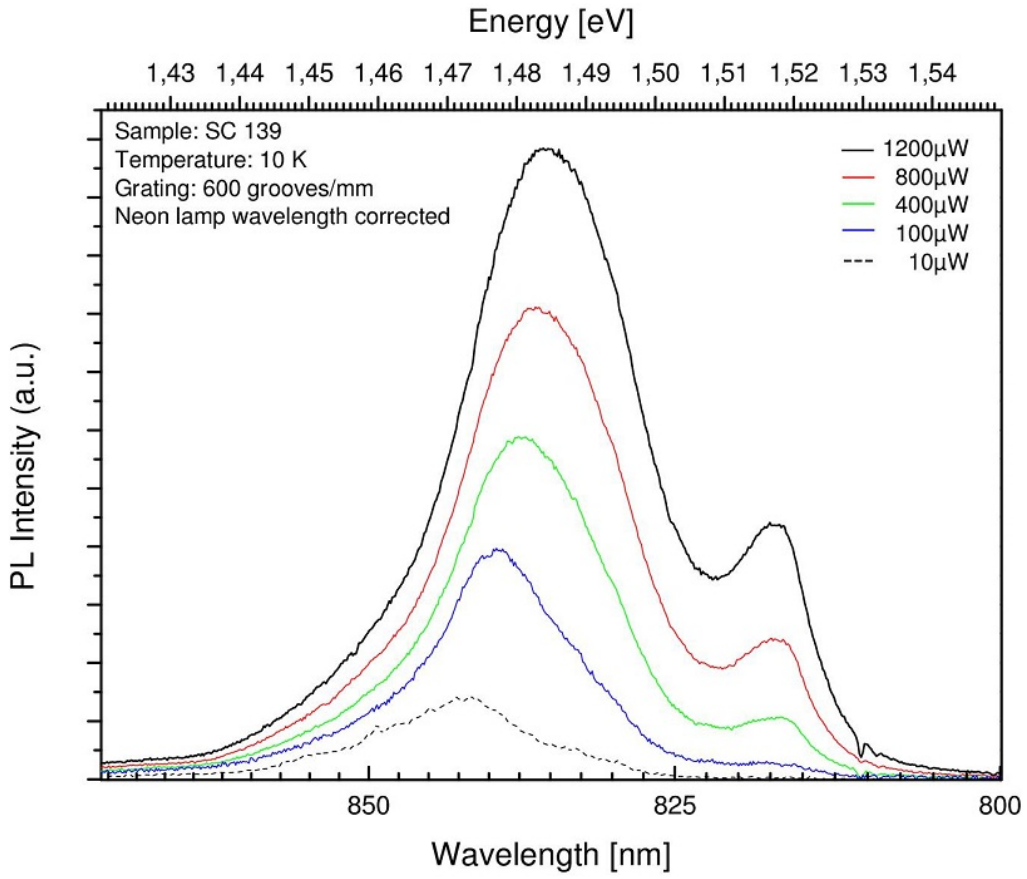

Figure 3.9: Peaks from macro-PL measurements done on SC-139 at 10 K are shown above.

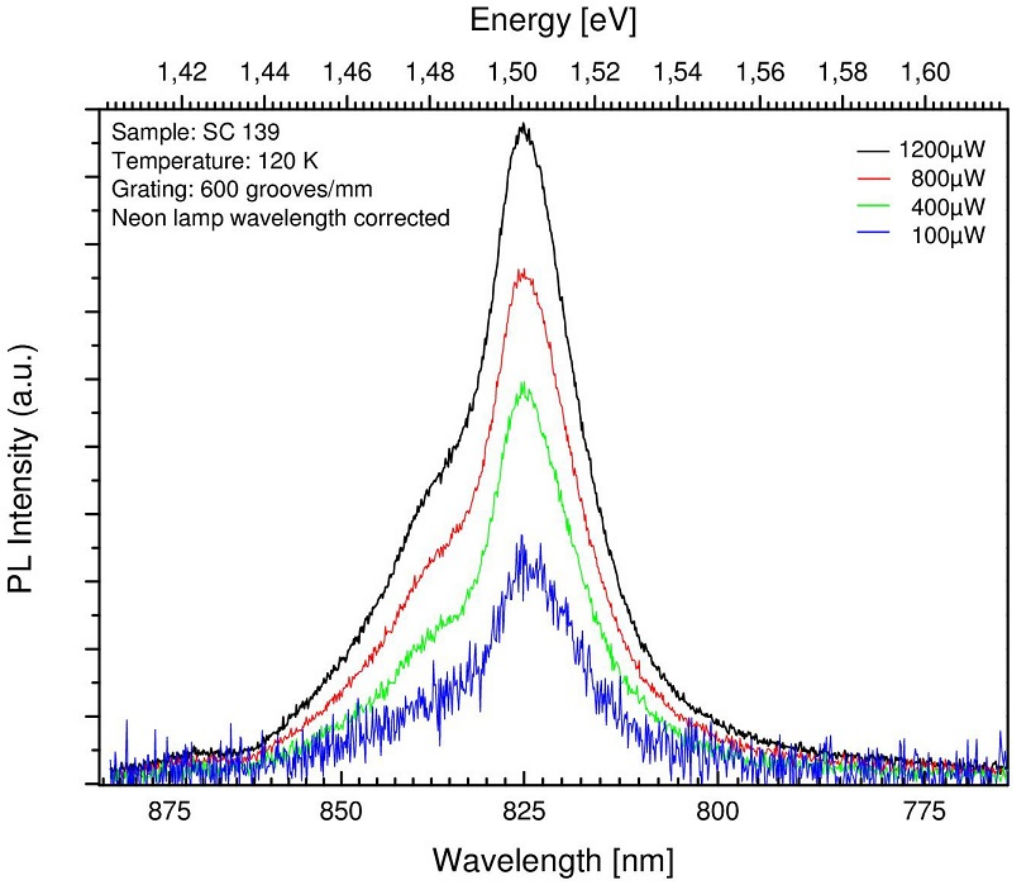

Figure 3.10: Peaks from macro-PL measurements done on SC-139 at 120 K are shown above. A modest PL intensity was observed for this sample, but no PL was detected below 100 μW excitation power at this temperature.

Figure 3.11 shows the peak positions at given temperatures for SC 139. These peak positions were obtained in the same way as for SC 109. Error bars were also here omitted due to very low error. The scatter plot was then fitted with the Varshni equation using the least mean squares method. Details of the fit is seen in the figure.

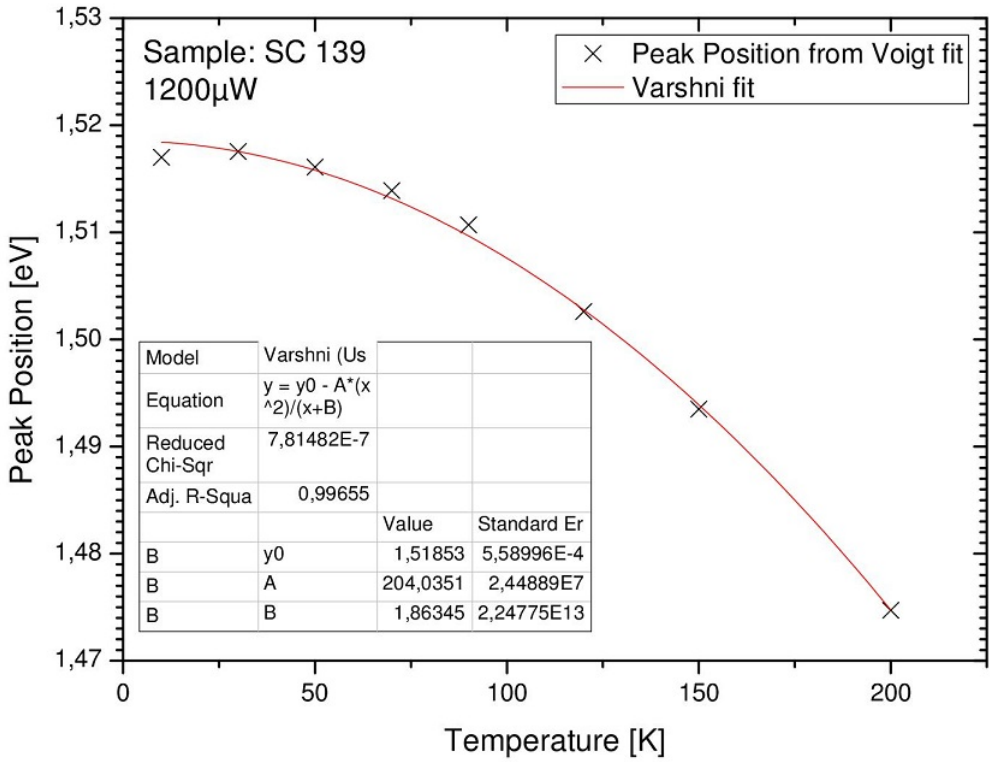

Figure 3.11: Scatter plot of peak positions of the strongest peak at different temperatures is shown above. Fitting was done using the Varshni equation in a least mean square sense. Details of the Varshni fit can be seen in the figure.

3.4 Measurements from sample SC-151

Overview of the measured macro-PL from sample SC-151 is shown in figures 3.12 and 3.13. The grating used is 600 grooves/mm, centered at 840 nm, with a 10 μm slit opening on the spectroscope. CCD exposure of 0.1 seconds at most excitation powers was used at 10 K, except for the three lowest intensities. Exposure of 1 second was used for all excitation powers at 150 K.

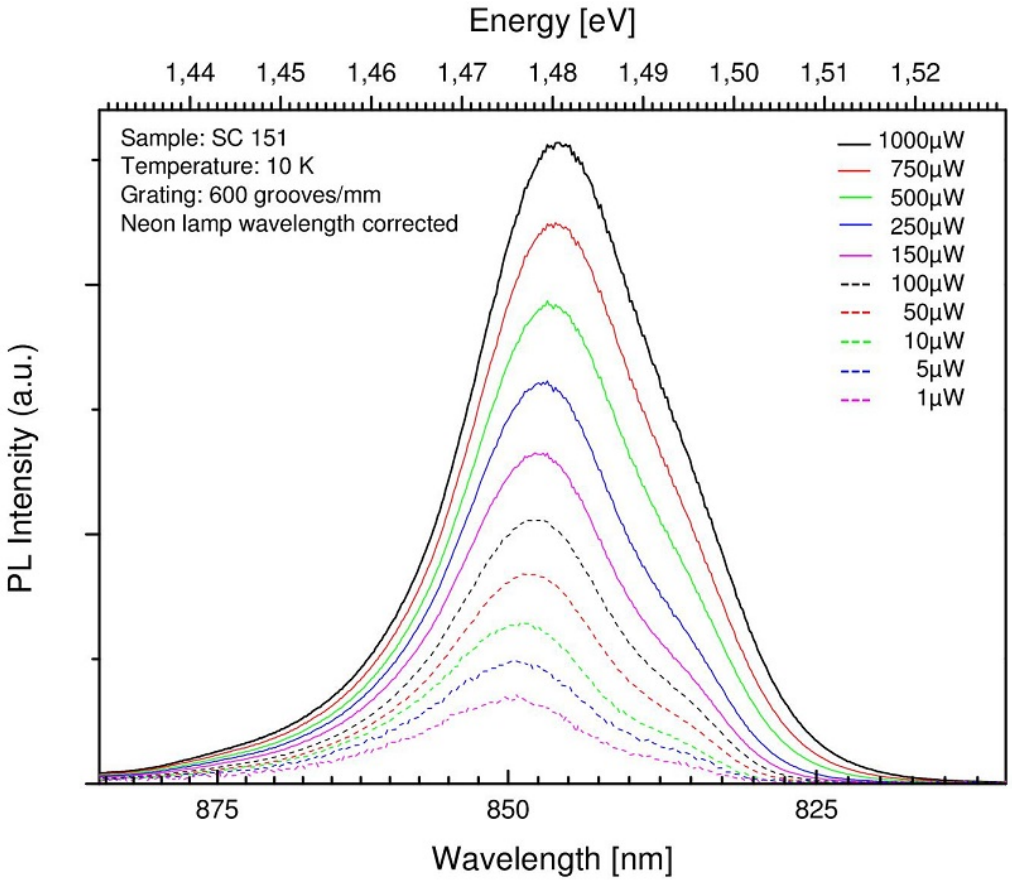

Figure 3.12: Peaks from macro-PL measurements done on SC-151 at 10 K are shown above.

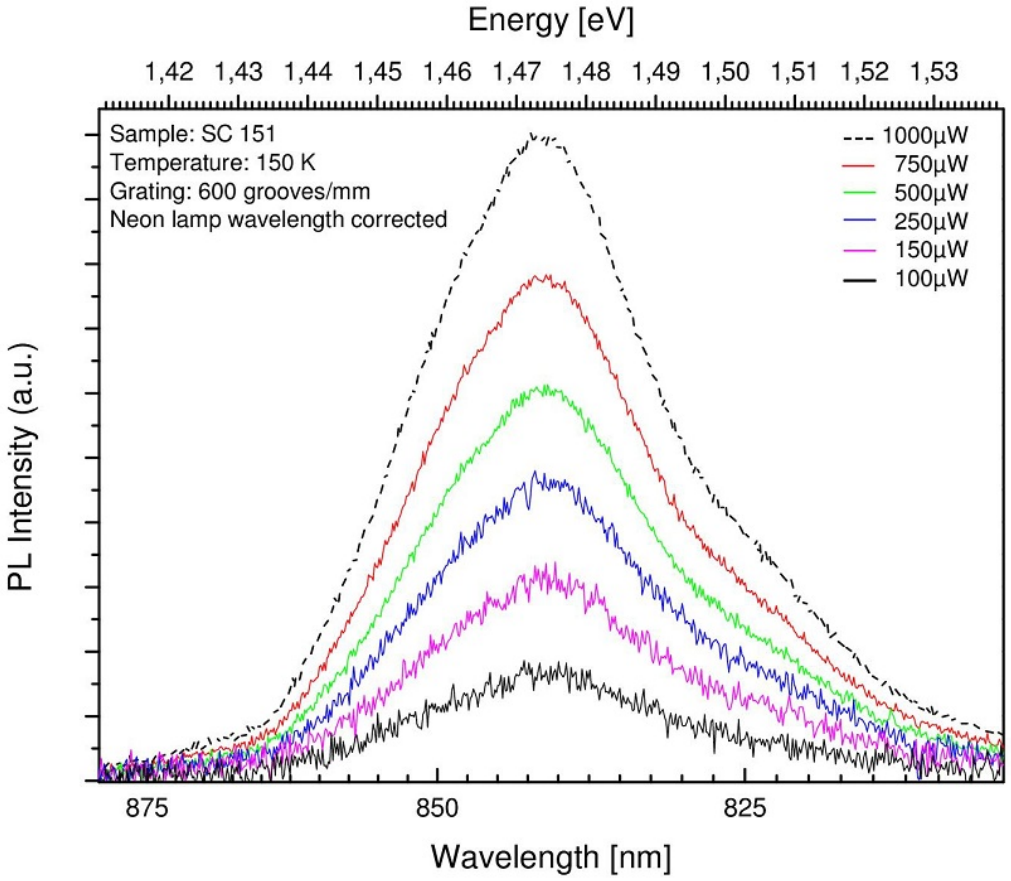

Figure 3.13: Peaks from macro-PL measurements done on SC-151 at 150 K are shown above. A decent PL intensity was observed for this sample, but no PL was detected at or below 100 μW excitation power at this temperature.

Measurements on single nanowires from sample SC-151 are presented in figures 3.14 and 3.15. Figure 3.14 presents measurements done at 9.6 K, using excitation powers somewhat less than used on the macro-PL measurements shown in figures 3.12 and 3.13. Measurements done at 150 K are shown in figure 3.15. The grating used in both cases has 300 grooves/mm.

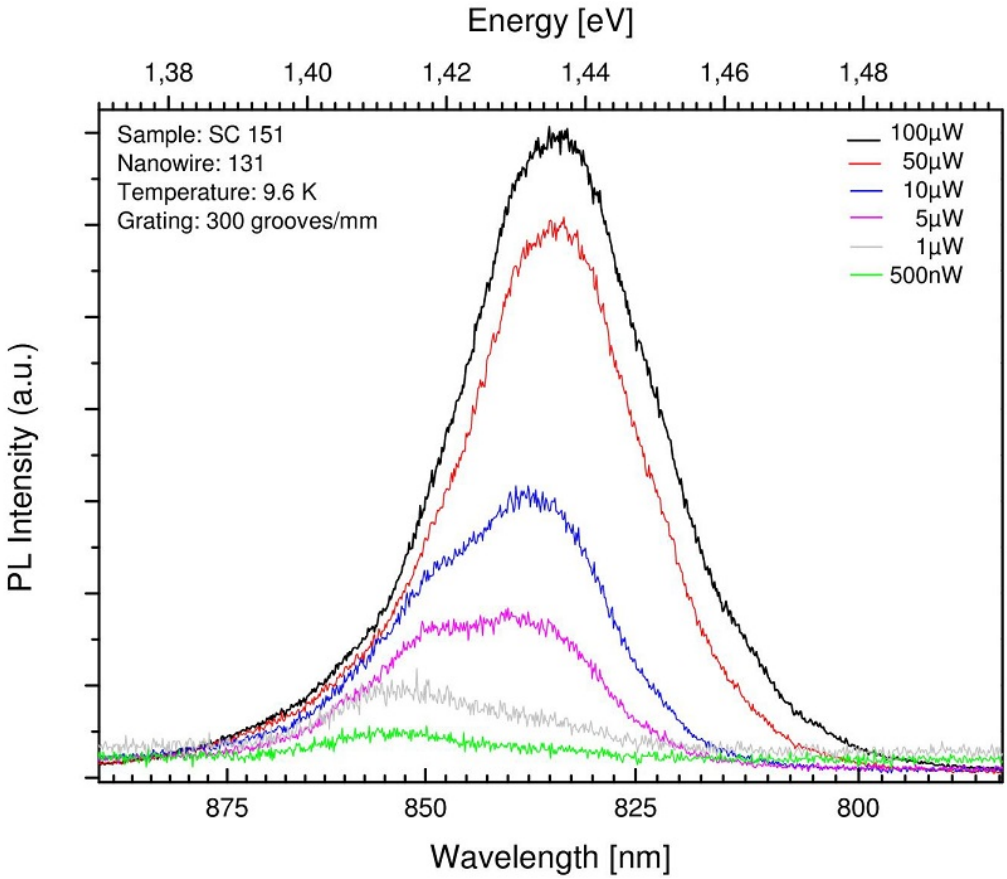

Figure 3.14: Measured μ-PL peaks from sample SC-151 done by Lyubomir Ahtapodov and Terje Sund Mjåland are shown above. The measurements were done at 9.6 K.

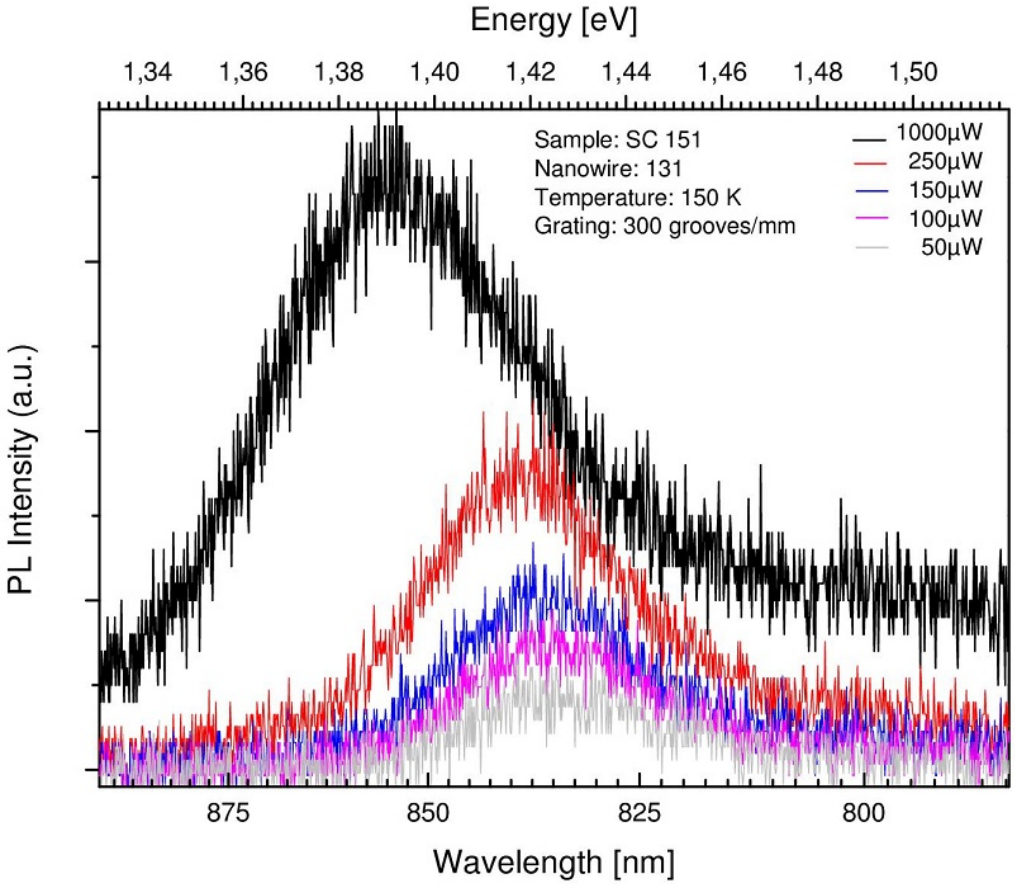

Figure 3.15: Measured μ-PL peaks from sample SC-151 done by Lyubomir Ahtapodov and Terje Sund Mjåland are shown above. The measurements were done at 150 K.

3.5 Measurements from sample SC-153

Overview of the measured macro-PL from sample SC-153 is shown in figures 3.16 and 3.17. The grating used is 600 grooves/mm, centered at 870 nm at 10 K and 860 nm at 290 K, with a 10 μm slit opening on the spectroscope. CCD exposure of 0.00001 seconds at most excitation powers was used at 10 K, while 1 second was used for all excitation powers at 290 K, except the two highest excitation powers. Fitted values give the PL peaks at positions summarized in table refTABLETABLE

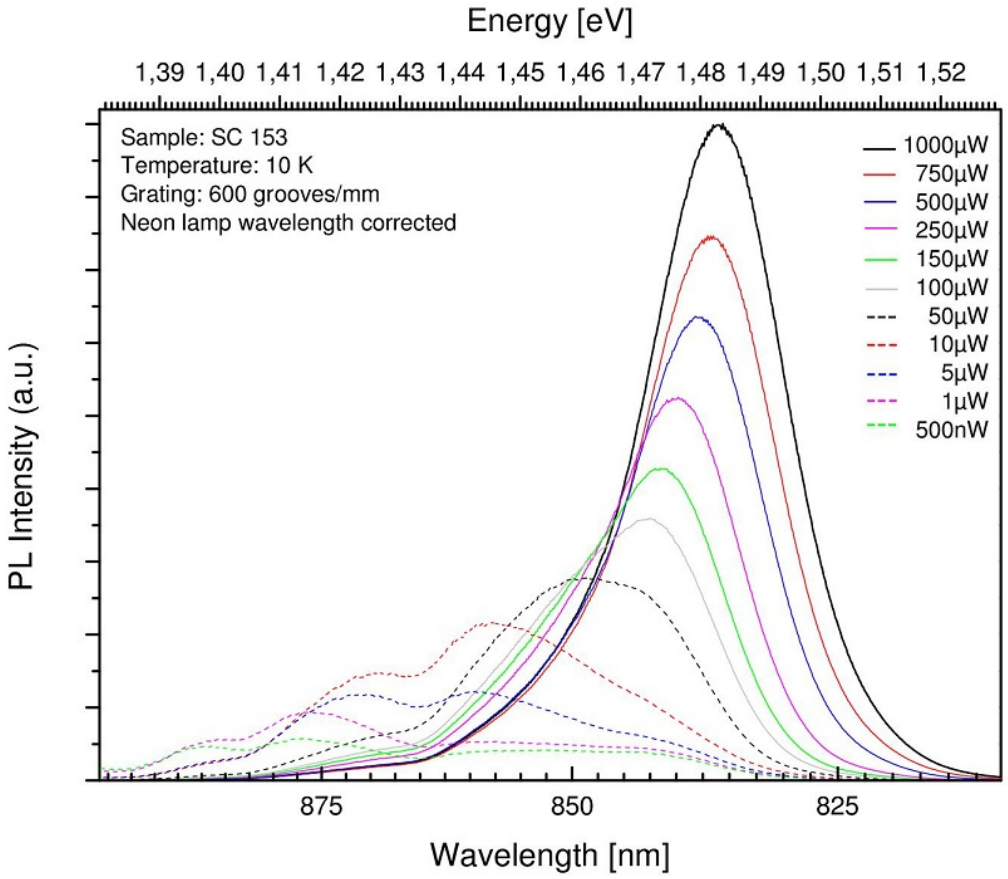

Figure 3.16: Peaks from macro-PL measurements done on SC-153 at 10 K are shown above.

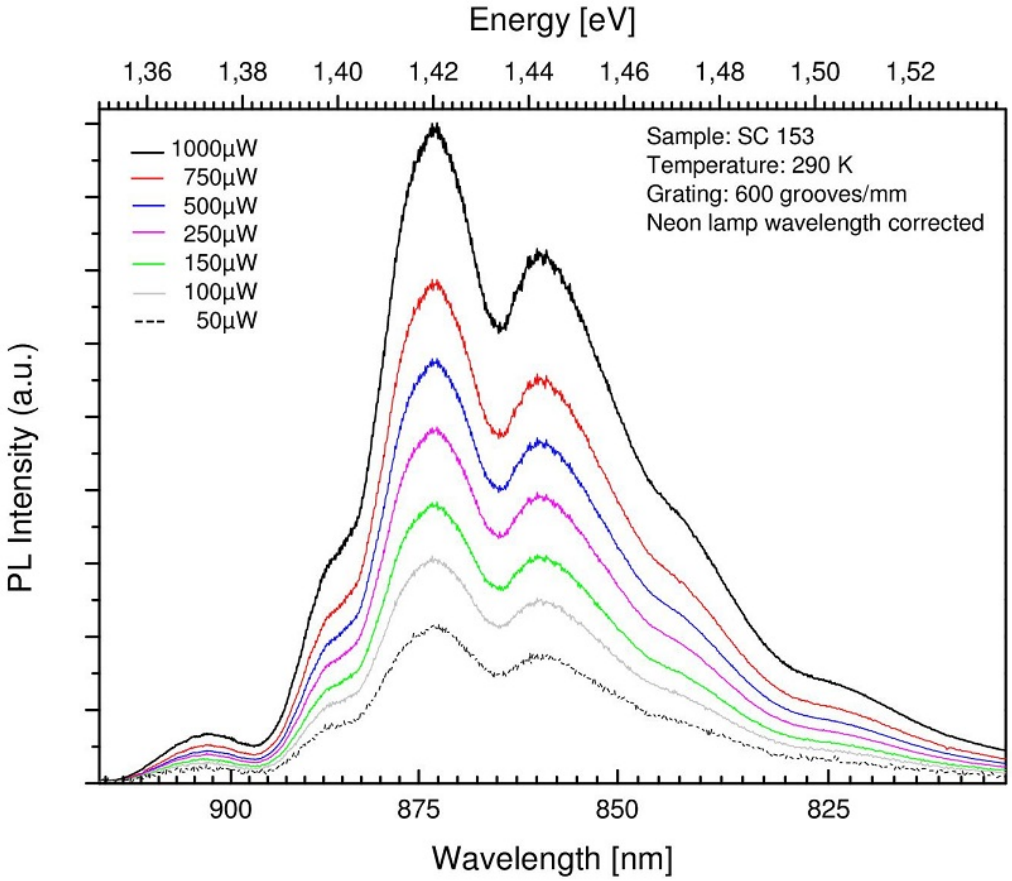

Figure 3.17: Peaks from macro-PL measurements done on SC-153 at 290 K are shown above. A very high PL intensity was observed for this sample, but no PL was detected at or below 10 μW excitation power at this temperature.

Measurements on single nanowires from sample SC-153 are presented in figures 3.18 and 3.19. Figure 3.18 presents measurements done at 10 K, using excitation powers somewhat less than used on the macro-PL measurements shown in figures 3.16 and 3.17. Measurements done at 290 K are shown in figure 3.19. The grating used in both cases has 300 grooves/mm.

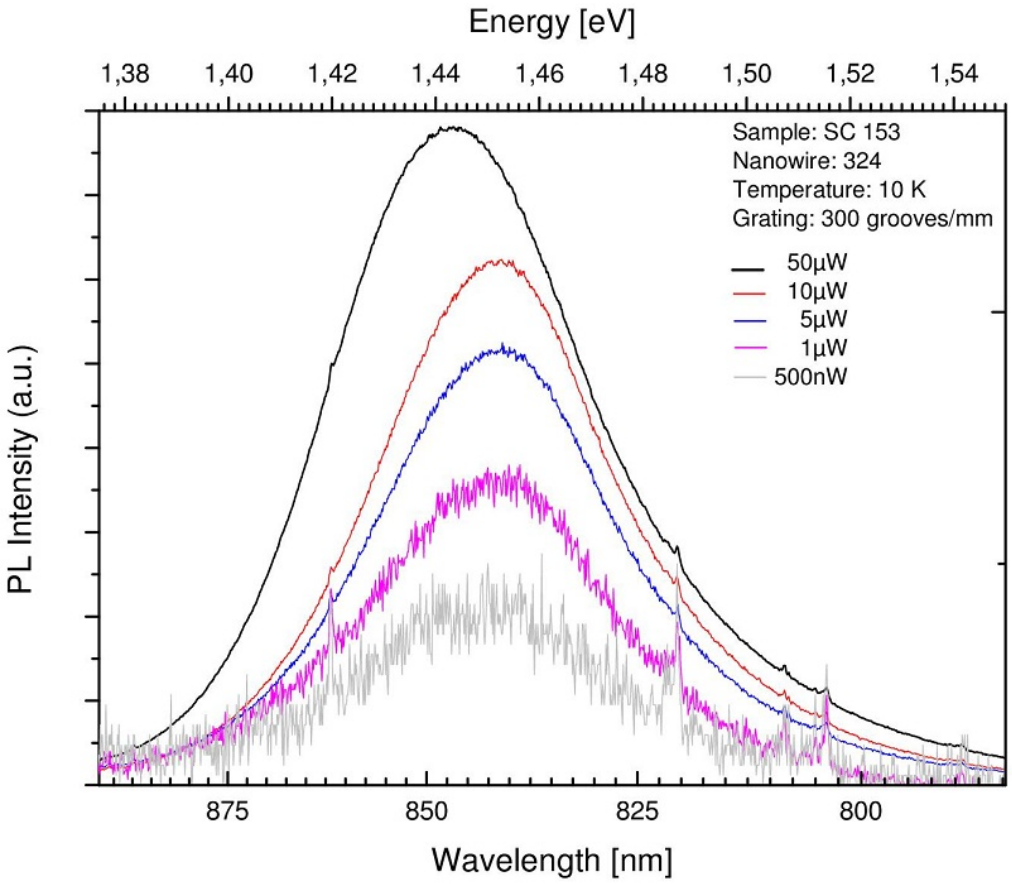

Figure 3.18: Measured μ-PL peaks from sample SC-153 done by Lyubomir Ahtapodov and Terje Sund Mjåland are shown above. The measurements were done at 10 K.

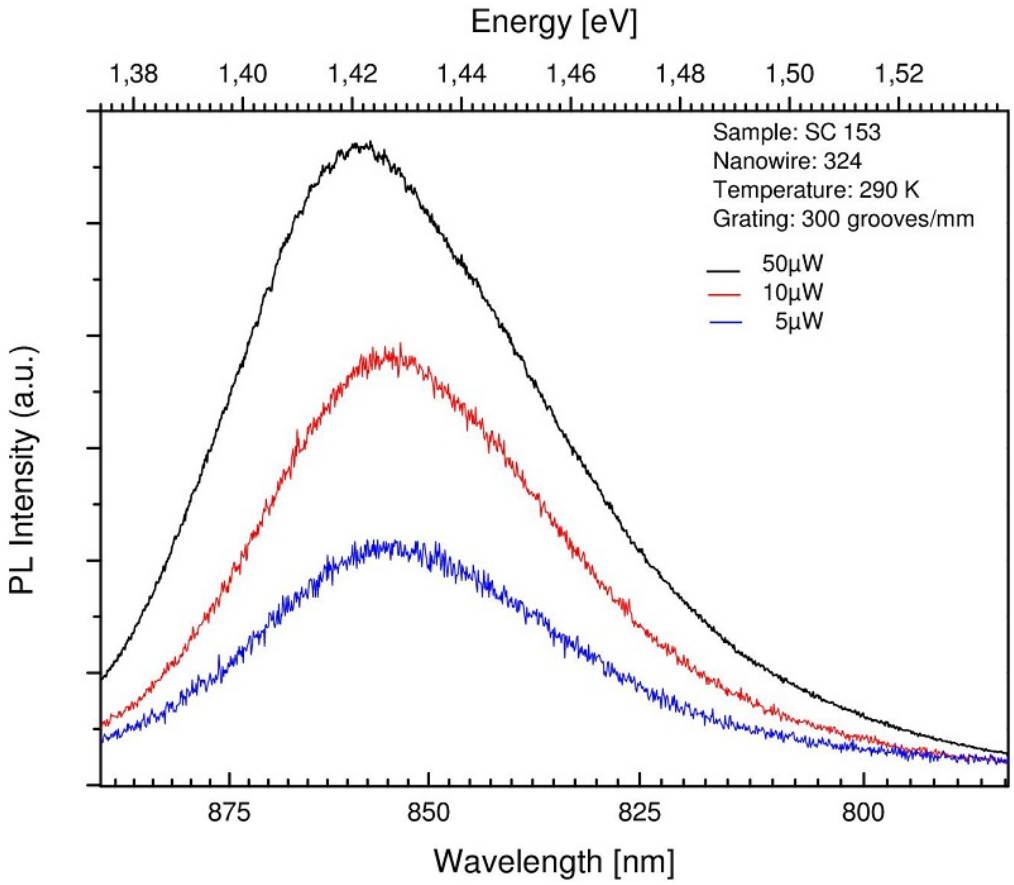

Figure 3.19: Measured μ-PL peaks from sample SC-153 done by Lyubomir Ahtapodov and Terje Sund Mjåland are shown above. The measurements were done at 290 K.

4 Discussion

The measured data introduces some interesting questions. The measurements will be discussed in the same order as they were presented in the last section. Remember that all samples are grown in a self-catalytic way, and that both core and core/shell samples have been investigated.

4.1 Sample SC-88

The first sample to be presented, SC-88, is a GaAs core type sample.

Since it is a GaAs core type sample, i.e. there is no shell for passivation, we expect a somewhat low observed PL intensity, especially at higher temperatures, and even when using relatively large excitation powers. From figure 3.2 this can indeed be seen. Not knowing what is considered to be a low PL intensity, it would be difficult to classify a sample accordingly. However, comparing the measurements to other samples being of core/shell type, it should be obvious, e.g. from measurements on sample SC-109 seen in figure 3.4 taken at 280 K. Macro-PL intensity from SC-88 diminished fast above a temperature of 100 K. The shell is not the only factor affecting PL intensity though. The amount of nanowires contributing to the observed PL would also affect its intensity. Using SEM images taken by the sample growers, in this case A.M. Munshi, knowing the approximate size of the laser spot on the sample and using the SEM images of the sample, it is possible to estimate how many nanowires contribute to the observed PL. For SC-88, with a laser spot diameter of approximately 30-40 μm, this amount is estimated to be in the range of 4-8000 nanowires. This is indeed a lot of nanowires contributing to a single measurement, represented by each of the single curves in the figures. One must assume that not all nanowires contribute in the same way, and not in the same intensity range. This high number of contributing nanowires brings forward an important point: the macro-PL measurements performed is a good indication of the overall quality and morphology of the grown nanowires.

With this in mind, looking at the measurements in figure 3.1 taken at 10 K, we see at least two peaks; the higher intensity peak at approximately 1.468 eV, shifting towards 1.46 eV at lower excitation powers. The weaker peak seems to be around 1.44 eV, not shifting appreciably with decreasing excitation power. These peaks are located at energies which is lower than the band gap of both ZB and WZ GaAs, thus it is likely that a type II transition is happening here. I.e. there is a type II band alignment due to an interface, e.g. one being of ZB GaAs and the other caused by e.g. a stacking fault. The excited electrons is thus found at the ZB conduction band edge, leading to recombination with holes, which are mostly found close to the stacking fault valence band edge. These must clearly exist in a very high density on this sample, since contributions from free exciton recombina-

tion are barely visible. Some contribution from free excitons could be represented in the right-most shoulder, seen in figure 3.1. Other groups have reported such red-shifting due to parts of the nanowire having a high density of twinning and ZB/WZ heterostructures, e.g. by M. Heiss et. al., [36].

At higher temperatures, seen in figure 3.2, the observed PL intensity at the same excitation powers has decreased appreciably. At the same time we see at least four peaks; two very weak and two of relatively strong intensity. These relatively strong ones are located at approximately 1.503 eV and at 1.478 eV. It is difficult to ascertain whether these peaks shift in energy, due to only two used excitation powers. At 110 K the Varshni equation gives us a theoretical ZB band gap of approximately 1.498 eV. Thus, the 1.503 eV peak may be due to carrier recombination at the ZB band gap, but this would suggest large errors in e.g. the temperature readout or the spectroscope. This is unlikely, and is discussed at the end of this chapter. This slight red-shift could be attributed to some average density of twinned layers in the nanowires mentioned above. The 1.478 eV peak is certainly lower than the ZB band gap at this temperature, but very close. This could possibly be from impurities or other states close to the band edge. Since the temperature here is 110 K, the thermal energy is approximately 9.5 meV, given by the product k_bT. Thus it is highly unlikely that any excitons participate in the observed PL. Assuming an exciton binding energy of 4.2 meV, the temperature limit for exciton thermalization is approximately 50 K. Thus, from now on, no excitons will be mentioned in the discussion of high temperature macro-PL measurements.

4.2 Sample SC-109

Next, SC-109 was presented. Both at low and relatively high temperatures a fairly strong PL intensity was observed. The estimated number of contributing nanowires is in the same range as for SC-88, i.e. 4-8000 nanowires. However, these nanowires are of a core/shell type. This means that non-radiative recombinations due to surface states of the core should be deactivated, and a higher PL intensity should be possible than without such a shell. Also, this should introduce recombinations from states of higher energy than the ZB GaAs bandgap due to the AlGaAs shell, and so we would expect such a peak in the measurements. This is indeed seen; in measurements taken at low temperature, as presented in figure 3.3, show a relatively weak peak located at approximately 1.585 eV. But this energy is too low; it is here assumed that the AlGaAs valence band edge is located 153 meV below the ZB GaAs valence band edge and the AlGaAs conduction band edge 240 meV above the ZB GaAs conduction band edge, thus the peak should be at approximately 1.67 eV. This is assuming the Al/Ga ratio is 0.3/0.7. The 1.585 eV peak could instead come from impurity related transitions in parts of the nanowire where the Al-content is substantially lower than expected or from the direct AlGaAs bandgap transitions with equally low Al-content. Blue-shifted GaAs transitions due to a ZB/WZ superlattice could also be possible [37]. Assuming

thin WZ layers, this question could be resolved by looking at the power dependent shift, but such dependence is not seen and the peak is thus attributed to AlGaAs bandgap transitions where the Al-content is quite low. This peak has disappeared at 280 K, as can be seen in figure 3.4. But as can be seen in both figures, the high PL intensity could be explained as being an effect of using shells on the nanowires.

The two strongest peaks seen at low temperatures can be found at approximately 1.522 eV and 1.508 eV at an excitation power of 1 mW. At decreasing power the 1.508 eV peak seems to be shifting towards lower energies; at 1 μW excitation power the peak can be found at approximately 1.485 eV. The 1.522 eV peak has disappeared at the lowest excitation power, but it does not seem to be shifting as the power is decreased. A shoulder is also seen, although its peak is difficult to locate accurately. It seems to be located below 1.5 eV at least. The 1.522 eV peak could be from free excitons generating light from the ZB GaAs bandgap transition, although its energy is a bit higher than expected. The 1.508 peak should come from confined states in some form.

Measurements done at higher temperatures, shown in figure 3.4, two peaks can be seen. One of them can be seen more clearly than the other. Also, at least three shoulders can be seen. The peak seen most clearly can be found at approximately 1.45 eV and it does not shift due to decreasing excitation power. The weakest peak, we could well call it the strongest shoulder, can be found at approximately 1.43 eV. This peak does not seem to shift either. The 1.43 eV peak could be from electron-hole recombination over the ZB bandgap. This is very close to earlier reported experimental values, summarized in [27]. The 1.45 eV peak could be from electron-hole recombination in long WZ crystal segments, very close to recently experimental, unpublished, WZ bandgap values by L. Ahtapodov et. al., [38]. It is strange, however, that this peak is higher in intensity than the ZB peak, since these wires should consist primarily of ZB crystal phase.

Comparing to measurements from two single nanowires from the same sample, as seen in figure 3.5 and 3.6, we see contributions from many different transitions. They all seem to be located below 1.5 eV, except for one of the shoulders at higher energies seen in figure 3.5. The strongest peak seen in the same figure at higher excitation power seems to be located at approximately 1.48 eV. In the other single nanowire measurement, presented in figure 3.6, the peak seems to be consisting of two rather closed spaced peaks around 1.46 and 1.47 eV. It is difficult to see a shift in these peaks when the excitation power is decreased, but the overall shape of the measured curve is strongly dependent on excitation power, which means that the observed intensity from each contributing bandgap transition depends differently on the power. These peaks found in the μ-PL measurements could be coming from the same sources as the weak shoulder seen in the macro-PL measurements, between 1.46 and 1.48 eV. In other words, the single nanowire could be untypical of the sample mean nanowire. Additionally, quite recent experiments done on single nanowires have reported such peaks and are thought to originate in areas with a

high density of twins and stacking faults, [36].

Additionally, μ-PL measurements from another sample, SC-138, are presented. It was thought to be sample SC-139, and that it thus could be compared to macro-PL measurements done on that sample, but later investigations revealed that the samples were different due to a misunderstanding between the experimenters. All measurements from both SC-138 and SC-139 were originally not included in this thesis. But SC-138 is very similar to SC-109 as discussed in section 3.2, and is thus discussed here. SC-139 are also presented in chapter 3, and discussed in the next section for completeness. From figure 3.7 we see a peak located at approximately 1.48 eV using high excitation power. This peak seems to be red-shifted at the highest excitation power compared to the other powers used, and only one shift seems to be visible. It could be attributed to nanowire heating due to a high power density. But the peaks are not found at ZB or WZ bandgap energies, which at this temperature should be found approximately at 1.52 eV. Peak position at lower excitation powers are found approximately at 1.49 eV, with a shoulder centered at 1.48 eV. The apparent red-shift at higher power is thus excluded as an explanation here.
Lastly, the peak positions from the strongest peak by doing macro-PL measurements at different temperatures on sample SC-109 is shown in figure 3.8. The resulting scatter plot was then fitted using the Varshni equation. A decent fit is observed, and with parameter values relatively close to GaAs bandgap values as reported earlier by Y. P. Varshni, [32], thus strengthening the assumption that this peak indeed represents transitions over the ZB GaAs bandgap.

4.3 Sample SC-139

Macro-PL measurements from SC-139 were then presented. These nanowires are bare GaAs cores, i.e. no shells are grown. Using the approximate density of wires on this sample, the number of contributing nanowires is estimated to be in the range 700 to 1400. Thus, it is surprising that this sample seems to be more bright, i.e. higher PL intensity observed, than SC-88, which had a lot more nanowires contributing. However, other factors could explain this, e.g. a laser spot size which differs between measurements on the different samples or a large number of contributing parasitic crystals, grown in between the nanowires during the growth scheme.

At low temperatures, two peaks are clearly seen, 3.9. Using 1.2 mW excitation power at 10 K, the peak of highest intensity seems to be located at 1.485 eV, while the other is found approximately at 1.517 eV. The 1.485 eV peak definitely shifts to lower energies with decreasing excitation power, while the 1.517 eV peak does not. This higher energy peak is thus probably due to free exciton recombination in the ZB bandgap, close to earlier reported values, [6]. The 1.485 eV peak may originate from twinning, similar to sample SC-109, but at a different density.

At higher temperatures the PL intensity diminishes quite fast, comparable to the SC-88 sample. Measurements done at 120 K with several excitation powers show one peak and one shoulder. The peak is located approximately at 1.502 eV. Using the Varshni equation gives a theoretical value of approximately 8 meV lower than this for the ZB GaAs transition. The Varshni equation could be slightly incorrect, but then we would have to assume a similar error every time we use it. Another explanation could be that the peak originates in long WZ segments, as the WZ GaAs bandgap is thought to be slightly wider, e.g. by studies performed by Murayama et. al. [33], but the size of the gap is a controversial subject due to the differing reports.

Figure 3.11 presents the scatter-plot on the location of the peak energies. A Varshni fit is then performed. Here the fitted parameters do not support the assumption that the peaks originate from the ZB bandgap. Some peaks of higher energy may fit as seen from the plot, but later peak positions may very well originate from other sources. As discussed above, the 1.502 peak at 120 K does not agree with the Varshni equation at that temperature, so we must assume that similar peaks at other temperatures have been mistaken as to originate from the ZB bandgap. It is included in this thesis to make this point clear, regardless of how badly it looks.

4.4 Sample SC-151

Next on the list of investigated samples is SC-151, a core type sample, i.e. no shell is grown for passivation of surface states. This is a particularly interesting sample due to the core being doped. This is not the first nanowire to be doped at NTNU, but the first investigated by the author. Note that all samples discussed have p-doped Si as substrate. Before measurements began it was assumed that a similar PL intensity would be observed as with other core-only samples at higher temperature, and necessarily darker than core/shell samples.

Figures 3.12 and 3.13 show the measurements at low and high temperatures, using different excitation powers. Indeed, the measurements seem to indicate that the observed intensity is comparable to e.g. SC-88 and SC-139 at higher temperatures, all being core-only samples. The observed difference in PL intensity is not great between SC-139 and SC-151. The number of nanowires contributing to the measurements done on SC-151 is estimated to be at least twice the number estimated for SC-139, easily seen when comparing the SEM images shown in the appendix. One can also see from the images that this difference could be even higher, but as SC-151 was next to the final measured sample, the laser spot size was improved during the course of all the measurements. This would mean a somewhat smaller spot size and thus lower number of contributing nanowires. All the same, this improvement was not very large, and it would not explain why SC-151 was a slightly brighter sample than SC-139. It is however difficult to ascertain with certainty on

such large sample investigations, as there are so many single nanowires of differing quality contributing to the mean signal observed. This is an important point that will be mentioned later.

Looking more closely at measurements from sample SC-151 at low and high temperatures, we see a very broad peak with at least one shoulder visible. A second shoulder at lower energies is possible to see at 10 K, as the curve falls off much slower here than at the high energy side of the peak. At higher temperatures this slow falling slope is found on the high energy side of the peak. The large and wide peak seems to be located at 1.481 eV at high excitation power done at 10 K, shifting slightly to lower energies as the power is decreased. A peak is found to be at approximately 1.474 eV at higher temperatures, with no appreciable shift at decreasing excitation powers. The slight red-shifting at decreasing power could be explained by the doping of the core. Such redshifted peaks have been reported before due to bandbending induced by Fermi-level pinning at the surface, [**?**], although these values were obtained from p-doped InP NWs.

Figures 3.14 and 3.15 show measurements done on a single nanowire at low and high temperature. This shows a different peak than seen in the macro-PL measurements. This could in fact be a nanowire dominated by type-II transitions from crystal defects, possibly contained in the slow falling slope seen in the macro-PL measurements done at low temperature, and thus not necessarily a typical example of the nanowires present on the sample. At higher temperatures, the peak seems to be blue-shifting as the power is decreased. Interestingly, the maximum power used here is 1 mW, a quite high power for μ-PL measurements. Assuming a spot size of 2 μm radius, the power density is approximately 8000 W/cm^2 with such an excitation power. The assumption that the radius of the focused laser spot is so high is quite conservative in the μ-PL setup used, so the power density may be much higher. This should lead to substantial heating of the nanowire and subsequent red-shifting at the highest power densities due to a narrower bandgap, also discussed in recent works by M. Heiss et. al., [36]. Such effects have also been seen in a study on InP nanowires by J. Bao et. al. [39]. Assuming direct fundamental band to band transitions in figure 3.15, we could estimate the temperature looking at the peak of lowest energy to be well above room temperature.

4.5 Sample SC-153

The last sample to be investigated is SC-153. This is a core/shell sample, but with both core and shell doped. The core is doped with Be and the shell is doped with Si ATCONCENTRATION?. Doping both the core and the shell in this manner should not lead to a large increase in observed PL intensity. It is however very important in optically excited nanowires for electrical measurements, as such doping would introduce a larger number of carriers contributing to the electrical characteristics. The PL intensity was expected to be very high at high temperatures due

the core/shell design, and this is also the case. The concentration of nanowires are more similar to SC-139 than SC-151, i.e. the number of contributing nanowires is approximately 2000 wires. Measurements done at low and high temperatures can be seen in figures 3.16 and 3.17 respectively.

At low temperature and high excitation power the peak is found at approximately 1.483 eV, with a shoulder barely seen at lower energies. This peak shifts appreciably towards the red with decreasing excitation power, almost disappearing at the lowest powers, with the shoulder peaks now dominating at energies at and below approximately 1.45 eV. These could originate from quantum confinement and type-II transitions. At higher temperatures we have a completely different situation, with two peaks clearly seen, and at least four contributing shoulder peaks. The two clearly seen peaks do not shift appreciably at decreasing excitation power, and are located at approximately at 1.42 and 1.444 eV. These two peaks may in fact come from electron-hole recombination over the bandgaps of ZB and WZ crystal phases respectively, as they are very similar to earlier reported values for the ZB bandgap, **??**, and a very recent unpublished study of WZ bandgaps by L. Ahtapodov et. al. **??**. This latest study even placed the WZ bandgap at 1.444 $\pm$ 1 meV at 294 K. Thus this peak may be due to extended WZ segments in most of the contributing nanowires in the macro-PL measurements. No peaks at the AlGaAs band gap was seen in any macro-PL measurement on this sample.

μ-PL study on a single nanowire from the same sample, shown in figures 3.18 and 3.19, show similar peaks as in the macro-PL measurements. I.e. peaks around 1.44 to 1.45 eV at low temperatures, and peaks around 1.42 eV at higher temperatures. Here we see a blue-shift in peak position between the highest and next highest excitation powers, specially at low temperature. This is similar to the μ-PL measurements done on SC-138, SC-151 and maybe even on one of the nanowires from SC-109. However, only the red-shift seen from μ-PL measurements done on SC-151 is consistent with bandgap narrowing of the ZB GaAs phase due to nanowire heating. All other μ-PL measurements are done with a maximum power approximately an order of magnitude lower. It could be explained by a laser spot that is focused on a different parts along the nanowire during measurements. However, this is unlikely since a similar shift is seen in the other single nanowire measurements mentioned above. It is thus unknown why we should get such an apparent red-shift using *higher* excitation power. Close to room temperature, the peak is seen as quite broad. One peak is clearly at approximately 1.42 eV, but a weak shoulder is seen around 1.44 eV. This could indeed be similar behavior as seen in the high temperature macro-PL measurements on the same sample, with two relatively strong peaks at these positions. It is concluded that these are the ZB and WZ bandgap transitions, where the WZ crystal phase may be of extended length in the wire.

Since no clear ZB or WZ bandgap energy is found at lower temperatures, no Varshni fit was performed on the peak positions seen from macro-PL measurements

on this sample.

4.6 About the measurements

There are probably many factors leading to errors in the measurements, but they are surprisingly low. Calculated errors from the spectrograph alone is below 1 meV in all measurements. This low value is achieved by correcting all measurements by using the neon lamp with tabulated values for the same spectrum at NIST, the National Institute of Standards and Technology. Thus the error in the peak positions primarily comes from the uncertainty in the fitted 3rd degree polynomial of the observed errors used in the correction of the spectrograph. The uncertainty of the fit lie within $\pm$ 0.01 nm using a 99 % confidence for the 600 grooves/mm grating, and at least an order of magnitude larger for the 150 grooves/mm grating. The 150 grating is not used in this thesis though, primarily because of increased spectral resolution of the 600 grating. Another factor leading to error are the measured temperatures. At 10 K, an estimated error lie within $\pm$ 0.1 K, with this error decreasing steadily at increasing temperature. These errors is not appreciable using the Varshni equation and are simply ignored. These are only in part systematic; at 10 K the feedback loop at the temperature controller can give some fluctuating temperature during operation. These fluctuations can be avoided though, if the user has appreciable knowledge about the correct feedback parameters, i.e. the constants P, I and D used in PID feedback loops. This is in practice not a difficult task, but it takes a lot of time.

There are also a small error calculated when fitting the curves with the Voigt distribution. The largest error observed in such a fit was $\pm$ 7.46 meV, a rather large error. But this peak was not used in any Varshni fit plot, neither in any discussion of observed peaks, primarily because it was difficult to see the same peak at higher excitation energies when it was probably a part of a shoulder. Error in peak position used in both the discussion and in the fitting of the Varshni equation lie within the range of 10^{-4}.

The single nanowire measurements give off quite different PL than observed during the macro-PL measurements at approximately the same temperatures. It is important to note that the excitation powers used in the macro- and μ-PL measurements are comparable in value, but the irradiance, or excitation power density, is completely different. In macro-PL measurements done during this thesis, a maximum of 1 mW was distributed among several thousand nanowires, i.e. over a relatively large area. In the μ-PL measurements on SC-109, 250 μW was used on a single nanowire. Also, in the μ-PL measurements, the laser beam is perpendicular on the nanowire axis, while it is parallel in the macro-PL measurements. This last point may be of paramount importance; in μ-PL measurements the experimenter may have full control over what parts of the nanowire is illuminated by the laser and thus, by comparable structural studies such as (S)TEM, the observed spectra could be attributed e.g. defect by direct structural observation. In macro-PL studies

such comparisons are not possible. In addition the laser is always hitting the top of the nanowire first, so we may very well be getting PL predominately from this part of the nanowire. This could explain why all macro-PL measurements presented in this thesis show large contributions from possible defects, as the top of the nanowire constitutes an critical area where such defects may be predominant. Also, in μ-PL measurements, the nanowires are broken off the as-grown sample. Thus, one suddenly has a new surface at the bottom of the nanowire that is not present in macro-PL measurements. This should undoubtedly lead to new states, possibly non-radiative ones, at this new nanowire/air interface. Comparisons done between macro- and μ-PL measurements done on the same type of sample should take this into account.

Also, in some of the measurements, specially at higher temperatures, it could be smart to add at least a few more excitation powers. This would give a better picture of the sample, e.g. the data presented in figure 3.2 could benefit from this. But the measurements were carried out following a rigid plan, where the laser power to be used was decided from measurements done at lower temperatures. This rigidity has in retrospect no real meaning, except of course by limiting the large amount of data gathered during an experiment, which could in fact be important, and making analysis more easy or difficult depending on the situation. It is also favorable to stop at a certain amount of measurements, as long as one thinks that enough data has been gathered. One could measure at closely spaced variable parameters if one wanted, e.g. at each integer temperature value, from 10 K to 290 K, making a single experiment over 280 measurements long. This is however not advantageous. There is a sweet spot in the correct spacing of e.g. temperature or excitation power between each measurement. This is often found after the experimental setup has been used several times and when the experimenter know the overall optical behavior of the samples to be investigated better. This is also the case in this thesis.

5 Conclusion

Doing macro-PL measurements on, not one, but several samples, generates a large volume of data to be interpreted. When doing μ-PL measurements on single nanowires, the researcher can be confident that it is only that particular nanowire contributing to the measured signal. When interpretations have been made, (S)TEM, or other suitable methods for structural characterization, can be performed to validate the points being made. This is not possible when measuring on a large ensemble of nanowires at once, as was done in this thesis. Then, the measured signal must be assumed to be an average of the whole, and can in principle be used to e.g. qualitatively define the quality of the sample under investigation. Interpretations made during the analysis of the data gathered from macro-PL measurements must bear in mind that there are thousands of nanowires contributing to the measured signal. If a certain peak is seen in many measurements on the same sample, and at the same time dominating over other observed peaks, one can make the assumption that many, or most, of the nanowires contributing to the signal contain transition(s) necessary for that particular peak to be visible. This does not mean that all the nanowires have these transitions though, leading one to question if a μ-PL measurement done on a single nanowire indeed represents the typical nanowire found on the as-grown sample. This conundrum is solved by doing a comparison between macro- and μ-PL measurements done on the same sample. Both macro- and μ-PL measurements have their strengths and weaknesses, but the most solid interpretations are made when the two methods are combined.

In this thesis we have seen the effects of the different types of nanowire samples on macro- and μ-PL measurements. Identification of the different peaks with absolute certainty has been difficult, in part due to their broad profile but also because structural characterizations of such a macro-samples are hard to do. But we do see some general characteristics which could be attributed to well known transitions; such as the ZB and WZ GaAs bandgaps, the AlGaAs bandgap and transitions due to twinned layers.

Future work could focus on similar investigations as done in this thesis, but with an additional type of μ-PL measurement; it would be very interesting to look at single nanowires from the top, i.e. with the laser beam parallel to the nanowire axis. If such a measurement was combined with both macro- and traditional μ-PL measurements, it would undoubtedly give very detailed information about the optical characteristics of the nanowire structure. Such nanowires would have to be grown on a patterned sample. The difficulty would then be to ascertain whether the nanowire investigated in the traditional μ-PL measurement is of the same type, i.e. with measurements done on a lying nanowire.

A.1

SEM images of the samples studied in this thesis are presented below. These were taken by Abdul Mazid Munshi, one of the growers in the Nanowire Group at NTNU.

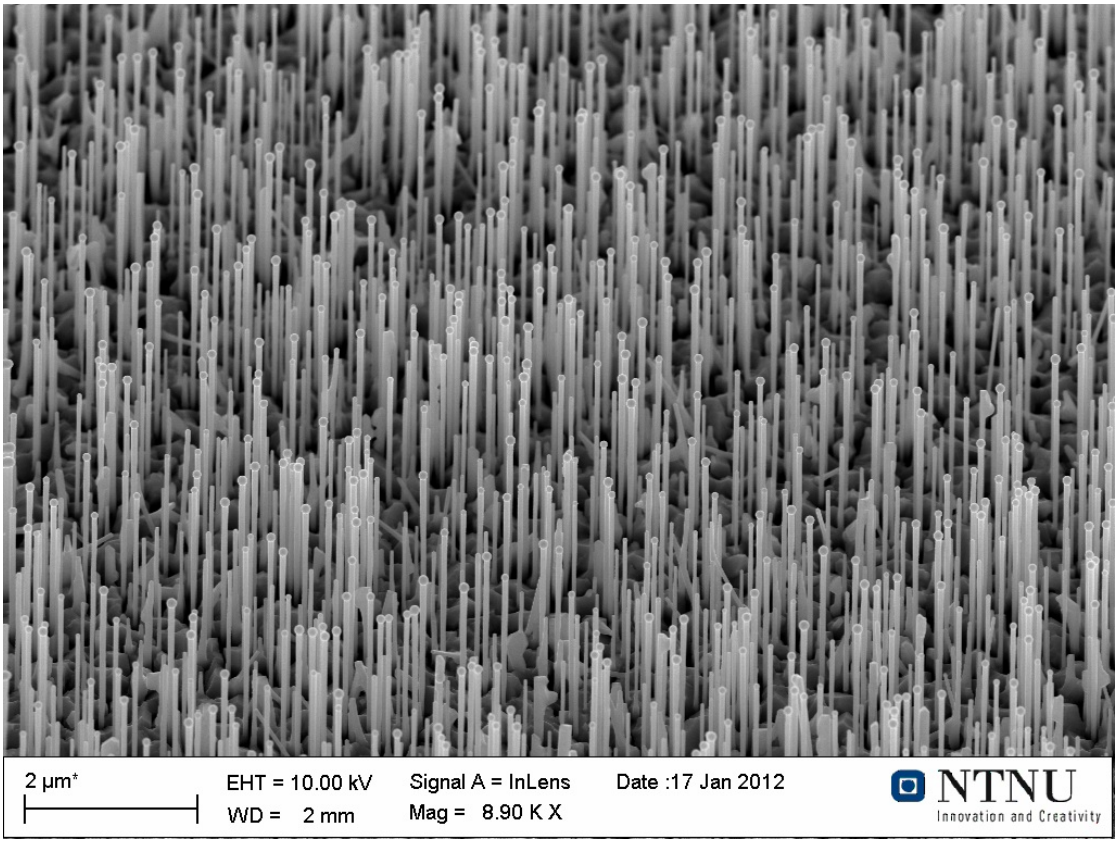

[
SEM image of SC-88]SEM image of sample SC-88 presented above, tilted at 45 degrees. Estimated density is 6.25 million per mm^2.

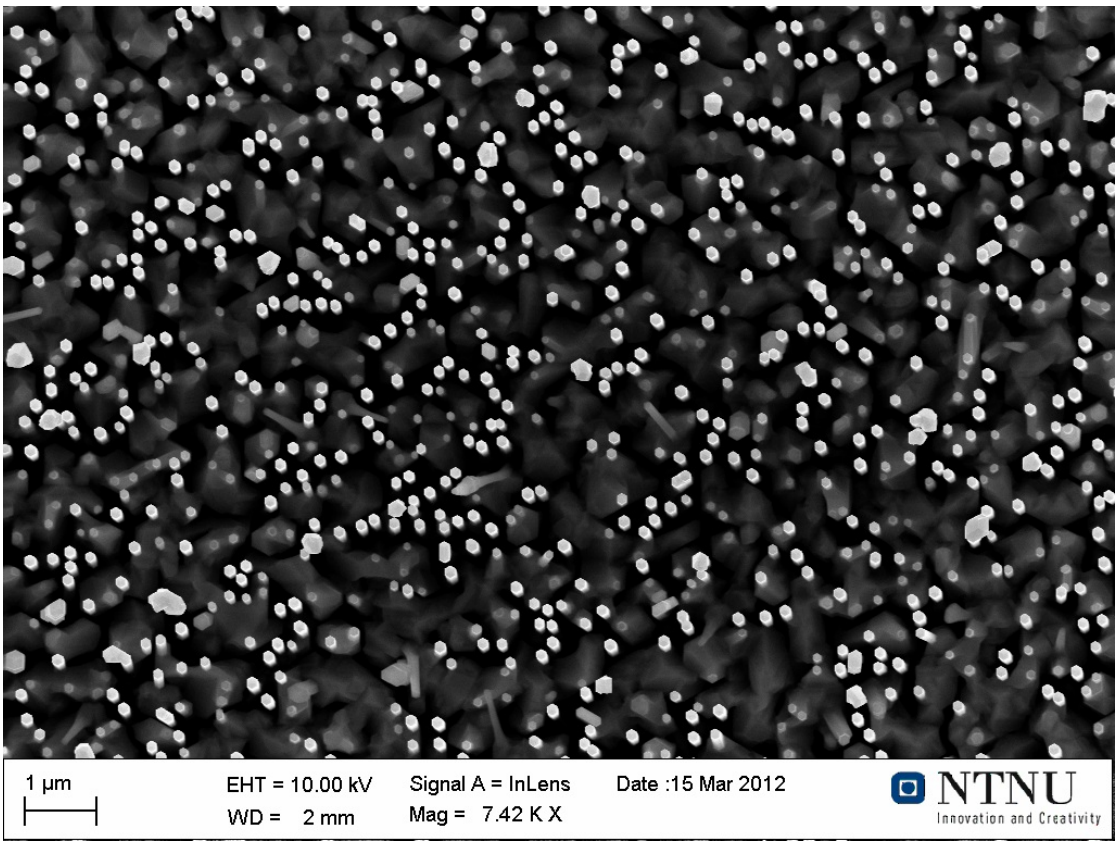

[
SEM image of SC-109]SEM image of sample SC-109 presented above, not tilted. Estimated density is 6.4 million per mm^2.

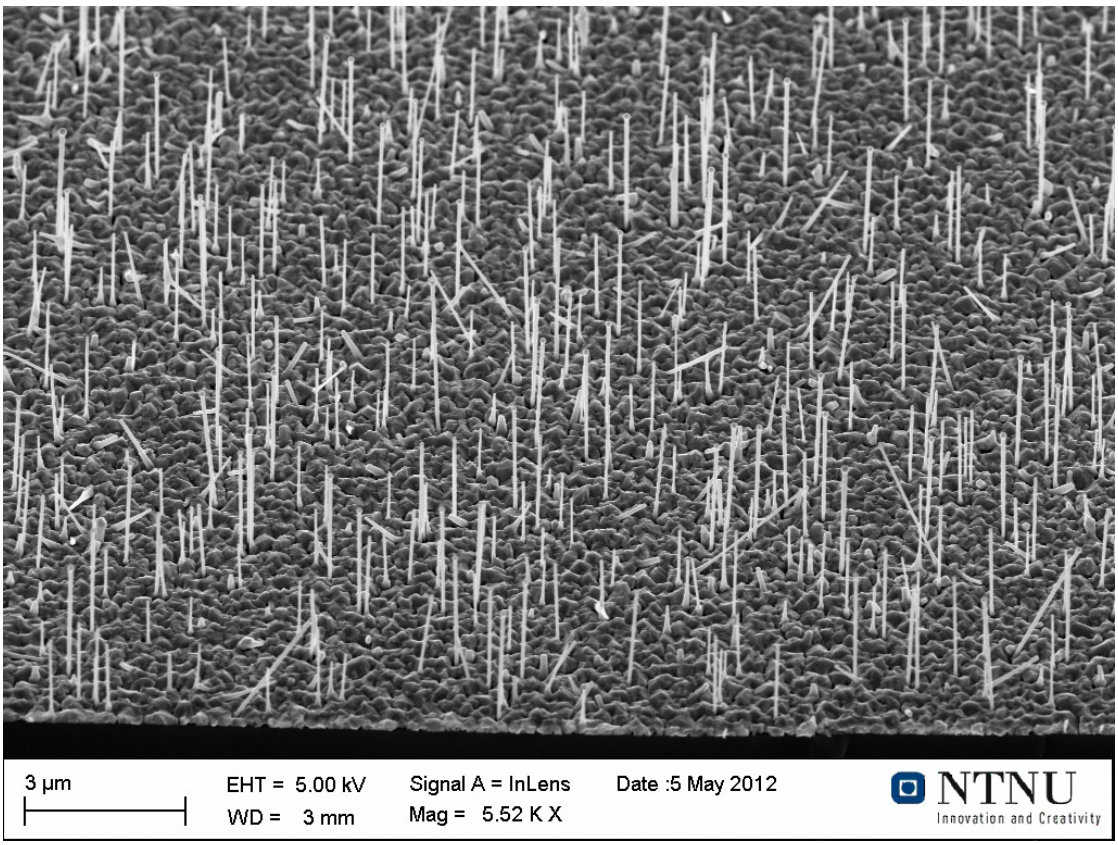

[
SEM image of SC-139]SEM image of sample SC-139 presented above, tilted at 45 degrees. Estimated density is 1.23 million per mm^2.

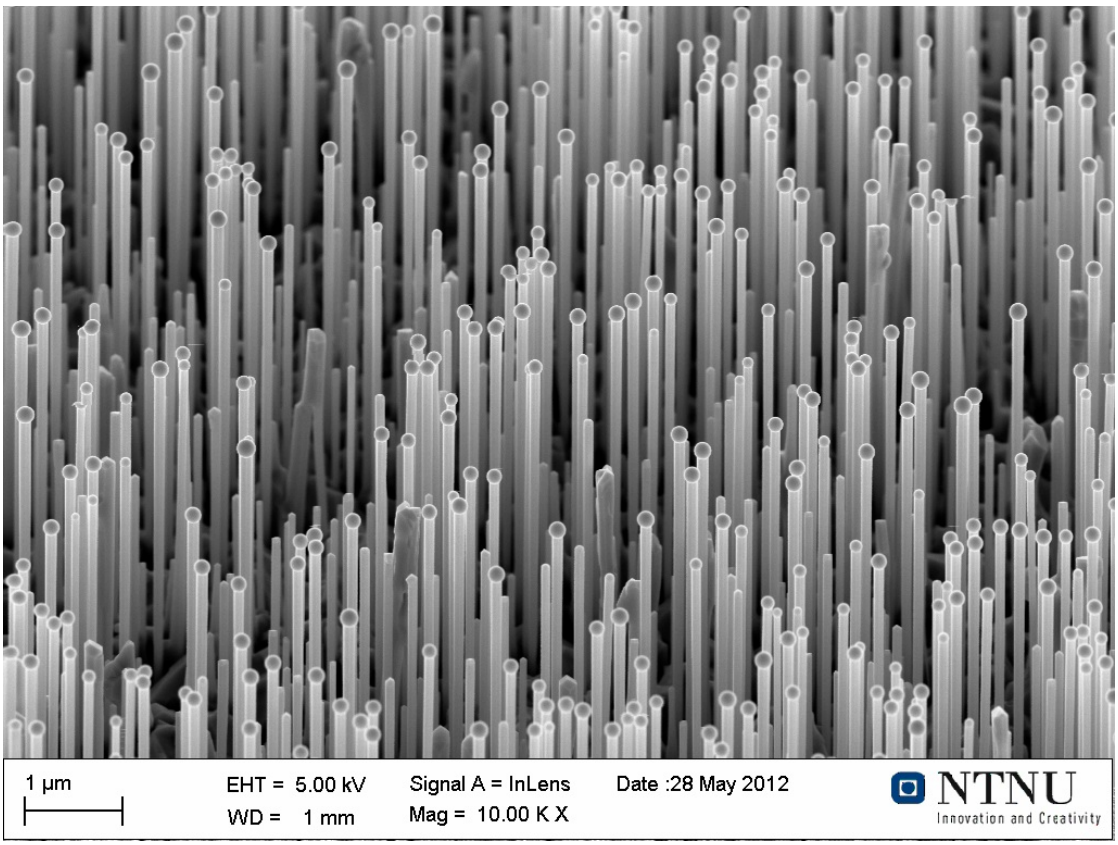

[
SEM image of SC-151]SEM image of sample SC-151 presented above, tilted at 45 degrees. Estimated density is 4 million per mm^2.

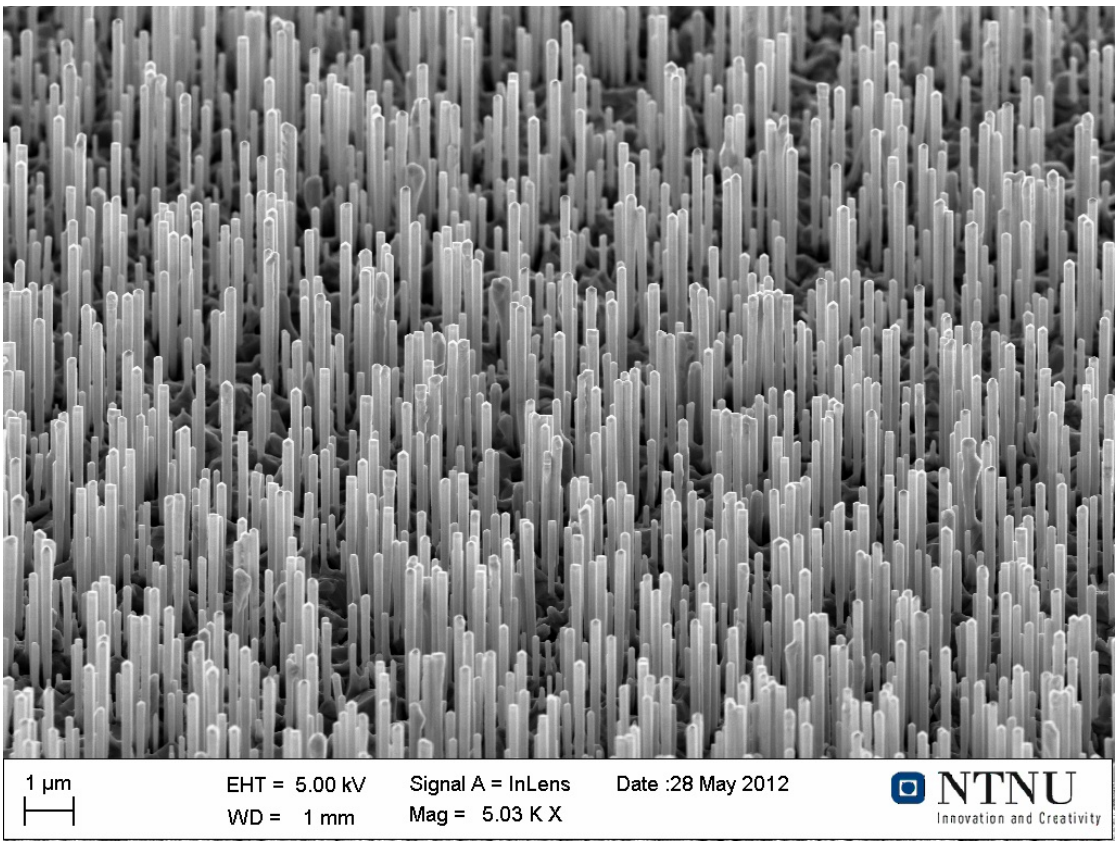

[
SEM image of SC-153]SEM image of sample SC-153 presented above, tilted at 45 degrees. Estimated density is 2.5 million per mm^2.

A.2

Details about the macro-PL measurements done on each sample are presented below.

[

Parameters from SC-88 macro-PL measurement]Parameters and details from macro-PL measurement done on SC-88

Cryostat vacuum during measurements, [mbar]	$1.1 \cdot 10^{-6}$
Used grating 1	150 grooves/mm, 800 nm blaze
Used grating 2	600 grooves/mm, 1000 nm blaze
Temperatures in measurement, [K]	10, 30, 50, 80, 110, 140
Excitation powers used, [μW]	1, 10, 100, 600, 1200
CCD camera exposures, [ms]	100 and 1000
Spectroscope slit opening, [μm]	40

[

Parameters from SC-109 macro-PL measurement]Parameters and details from macro-PL measurement done on SC-109

Cryostat vacuum during measurements, [mbar]	$3 \cdot 10^{-6}$
Used grating 1	150 grooves/mm, 800 nm blaze
Used grating 2	600 grooves/mm, 1000 nm blaze
Temperatures in measurement, [K]	10-110 in steps of 20, 140
Excitation powers used, [μW]	0.5, 1, 10, 100-1000 at steps of 100
CCD camera exposures, [ms]	10 and 500
Spectroscope slit opening, [μm]	10

[

Parameters from SC-139 macro-PL measurement]Parameters and details from macro-PL measurement done on SC-139

Cryostat vacuum during measurements, [mbar]	$2.7 \cdot 10^{-6}$
Used grating 1	150 grooves/mm, 800 nm blaze
Used grating 2	600 grooves/mm, 1000 nm blaze
Temperatures in measurement, [K]	10-90 in steps of 20, 120, 150, 200
Excitation powers used, [μW]	1, 10, 100, 400-1200 in steps of 400
CCD camera exposures, [ms]	120 and 1000
Spectroscope slit opening, [μm]	70

[

Parameters from SC-151 macro-PL measurement]Parameters and details from macro-PL measurement done on SC-151

Cryostat vacuum during measurements, [mbar]	$1.2 \cdot 10^{-6}$
Used grating 1	150 grooves/mm, 800 nm blaze
Used grating 2	600 grooves/mm, 1000 nm blaze
Temperatures in measurement, [K]	10-100 in steps of 25. 150 and 200
Excitation powers used, [μW]	1, 5, 10, 50-150 in steps 50. 250-1000 in steps of 250.
CCD camera exposures, [ms]	100 and 1000
Spectroscope slit opening, [μm]	10

[

Parameters from SC-153 macro-PL measurement]Parameters and details from macro-PL measurement done on SC-153

Cryostat vacuum during measurements, [mbar]	$9.3 \cdot 10$
Used grating 1	150 grooves/mm, 800 nm bla
Used grating 2	600 grooves/mm, 1000 nm bla
Temperatures in measurement, [K]	10-100 in steps of 25. 150-250 in steps of 50. 29
Excitation powers used, [μW]	0.5, 1, 5, 10, 50-150 in steps 50. 250-1000 in steps of 25
CCD camera exposures, [ms]	0.01, 100 and 10
Spectroscope slit opening, [μm]	

Bibliography

[1] J. Galván-Moya, W. Gutiérrez, and C. Moscoso, "Binding Energy of Exciton in a Nanowire Superlattice in Magnetic and Electric Fields," *Journal of Physics: Conference Series*, vol. 210, 2010.

[2] R. Elliott, "Intensity of Optical Absorption by Excitons," *Physical Review*, vol. 108, pp. 1384–1389, 1957.

[3] F. Glas, J. Harmand, and G. Patriarche, "Why Does Wurtzite Form in Nanowires of III-V Zinc Blende Semiconductors," *Physical Review Letters*, vol. 99, 2007.

[4] J. Harmand, G. Patriarche, N. Péré-Laperne, M.-N. Mérat-Combes, and L. Travers, "Analysis of Vapor-Liquid-Solid Mechanism in Au-Assisted GaAs Nanowire Growth," *Applied Physics Letters*, vol. 87, 2005.

[5] X. Zhang, X. Zhang, K. Zou, C.-S. Lee, and S.-T. Lee, "Single-Crystal Nanoribbons, Nanotubes, and Nanowires from Intramolecular Charge-Transfer Organic Molecules," *Journal of American Chemical Society*, vol. 129, pp. 3527–3532, 2007.

[6] G. Gilliland, "Photoluminescence Spectroscopy of Crystalline Semiconductors," *Material Science and Engineering: Reports*, vol. 18, pp. 99–399, 1997.

[7] J. Johnson, H. Yan, R. Schaller, L. Haber, R. Saykally, and P. Yang, "Single Nanowire Lasers," *The Journal of Physical Chemistry B*, vol. 105, pp. 11387–11390, 2001.

[8] X. Duan, Y. Huang, R. Agarwal, and C. Lieber, "Single-Nanowire Electrically Driven Lasers," *Nature*, vol. 421, pp. 241–245, 2003.

[9] F. Patolsky, G. Zheng, and C. Lieber, "Nanowire-Based Biosensors," *Analytical Chemistry*, vol. 78, pp. 4260–4269, 2006.

[10] T. Hoang, A. Moses, H. Zhou, D. Dheeraj, B. Fimland, and H. Weman, "Observation of Free Exciton Photoluminescence Emission From Single Wurtzite GaAs Nanowires," *Applied Physics Letters*, vol. 94, 2009.

[11] D. Dheeraj, G. Patriarche, L. Largeau, H. Zhou, A. van Helvoort, F. Glas, J. Harmand, B.-O. Fimland, and H. Weman, "Zinc Blende GaAsSb Nanowires Grown by Molecular Beam Epitaxy," *Nanotechnology*, vol. 19, 2008.

[12] W. Lu, P. Xie, and C. Lieber, "Nanowire Transistor Performance: Limits and Applications," *IEEE Transactions on Electron Devices*, vol. 55, pp. 2859–2876, 2008.

[13] R. Wagner and W. Ellis, "Vapor-Liquid-Solid Mechanism of Single Crystal Growth," *Applied Physics Letters*, vol. 4, pp. 89–90, 1964.

[14] Y. Wu and P. Yang, "Direct Observation of Vapor-Liquid-Solid Nanowire Growth," *Journal of American Chemical Society*, vol. 123, pp. 3165–3166, 2001.

[15] S. Plissard, G. Larrieu, X. Wallart, and P. Caroff, "High Yield of Self-Catalyzed GaAs Nanowire Arrays Grown on Silicon via Gallium Droplet Positioning," *Nanotechnology*, vol. 22, 2011.

[16] M. McMahon and R. Nelmes, "Observation of a Wurtzite Form of Gallium Arsenide," *Physical Review Letters*, vol. 95, p. 215505, 2005.

[17] M. Brozel and G. Stillman, *Properties of Gallium Arsenide*. INSPEC, The Institution of Electrical Engineers, 3 ed., 1996. 0-85296-885-X.

[18] B. Bauer, A. Rudolph, M. Soda, A. i Morral, J. Zweck, D. Schuh, and E. Reiger, "Position Controlled Self-Catalyzed Growth of GaAs Nanowires by Molecular Beam Epitaxy," *Nanotechnology*, vol. 21, p. 435601, 2010.

[19] D. Dheeraj, G. Patriarche, H. Zhou, T. Hoang, A. Moses, S. Grønsberg, A. van Helvoort, B.-O. Fimland, and H. Weman, "Growth and Characterization of Wurtzite GaAs Nanowires with Defect-Free Zinc Blende GaAsSb Inserts," *Nano Letters*, vol. 8, pp. 4459–4463, 2008.

[20] M. Plante and R. LaPierre, "Au-assisted Growth of GaAs Nanowires by Gas Source Molecular Beam Epitaxy: Tapering, Sidewall Faceting and Crystal Structure," *Journal of Crystal Growth*, vol. 310, pp. 356–363, 2008.

[21] M. Galicka, M. Bukala, R. Buczko, and P. Kacman, "Modelling the Structure of GaAs and InAs Nanowires," *Journal of Physics: Condensed Matter*, vol. 20, 2008.

[22] T. Akiyama, K. Sano, K. Nakamura, and T. Ito, "An Empirical Potential Approach to Wurtzite-Zinc Blende Polytypism in Group III-V Semiconductor Nanowires," *Japanese Journal of Applied Physics*, vol. 45, p. L275, 2006.

[23] J.-H. Kang, Q. Gao, H. Joyce, H. Tan, C. Jagadish, Y. Kim, Y. gao, H. Xu, J. Zou, M. Fickenscher, L. Smith, H. Jackson, and J. Yarrison-Rice, "Defect-Free GaAs/AlGaAs Core-Shell Nanowires on Si Substrates," *Crystal Growth and Design*, vol. 11, pp. 3109–3114, 2011.

[24] L. Titova, T. Hoang, H. Jackson, L. Smith, J. Yarrison-Rice, Y. Kim, H. Joyce, H. Tan, and C. Jagadish, "Temperature Dependence of Photoluminescence From Single Core-Shell GaAs-AlGaAs Nanowires," *Applied Physics Letters*, vol. 89, 2006.

[25] J. Walter and M. Cohen, "Calculation of the Reflectivity, Modulated Reflectivity, and Band Structure of GaAs, GaP, ZnSe, and ZnS," *Physical Review*, vol. 183, pp. 763–772, 1969.

[26] A. De and C. Pryor, "Predicted Band Structures of III-V Semiconductors in the Wurtzite Phase," *Physical Review B*, vol. 81, 2010.

[27] F. Duan and J. Guojun, *Introduction to Condensed Matter Physics: Volume 1*, vol. 1. World Scientific Publishing, 1 ed., 2005. 981-238-711-0.

[28] Z. Zanolli, F. Fuchs, J. Furthmüller, U. von Barth, and F. Bechstedt, "Model GW Band Structure of InAs and GaAs in the Wurtzite Phase," *Physical Review B*, vol. 75, 2007.

[29] S. Sze and K. Ng, *Physics of Semiconductor Devices*. John Wiley and Sons, Inc, 3 ed., 2007. 978-0-471-14323-9.

[30] S. Adachi, *Properties of Aluminum Gallium Arsenide*, vol. 1. INSPEC, Institution of Electrical Engineers, 1 ed., 1993. 0-85296-558-3.

[31] W. Wang, "On the Band Offsets of AlGaAs/GaAs and Beyond," *Solid-State Electronics*, vol. 29, pp. 133–139, 1986.

[32] Y. Varshni, "Temperature Dependence of the Energy Gap in Semiconductors," *Physica*, vol. 34, pp. 149–154, 1967.

[33] M. Murayama and T. Nakayama, "Chemical Trend of Band Offsets at Wurtzite/Zinc-Blende Heterocrystalline Semiconductor Interfaces," *Physical Review B*, vol. 49, pp. 4710–4724, 1994.

[34] B. Ketterer, M. Heiss, E. Uccelli, J. Arbiol, and A. Morral, "Untangling the Electronic Band Structure of Wurtzite GaAs Nanowires by Resonant Raman Spectroscopy," *ACS Nano*, vol. 5, pp. 7585–7592, 2011.

[35] S. Taguchi, T. Goto, M. Takeda, and G. Kido, "Magneto-Optical Effects of the Wannier Exciton in a Biaxial ZnP_2 Crystal," *Journal of the Physical Society of Japan*, vol. 57, pp. 3256–3261, 1988.

[36] M. Heiss, S. Conesa-Boj, J. Ren, H. Tseng, A. Gali, A. Rudolph, E. Uccelli, F. Peiró, J. Morante, D. Schuh, E. Reiger, E. Kaxiras, J. Arbiol, and A. Morral, "Direct Correlation of Crystal Structure and Optical Properties in Wurtzite/Zinc-Blende GaAs Nanowire Heterostructures," *Physical Review B*, vol. 83, p. 045303, 2011.

[37] L. Zhang, J. Luo, A. Zunger, N. Akopian, V. Zwiller, and J. Harmand, "Wide InP Nanowires with Wurtzite/Zincblende Superlattice Segments Are Type-II whereas Narrower Nanowires Become Type-I: An Atomistic Pseudopotential Calculation," *Nano Letters*, vol. 10, pp. 4055–4060, 2010.

[38] L. Ahtapodov, J. Todorovic, P. Olk, T. Mjåland, P. Slåttnes, D. Dheeraj, and A. van Helvoort, "A Story Told by a Single Nanowire: Wurtzite GaAs and Optical Quality Achievable with Au-assisted MBE Growth," *Unpublished/-Manuscript*, 2012.

[39] J. Bao, D. Bell, and F. Capasso, "Optical Properties of Rotationally Twinned InP Nanowire Heterostructures," *Nano Letters*, vol. 8, pp. 836–841, 2008.

[40] H. Zhou, T. Hoang, D. Dheeraj, A. van Helvoort, L. Liu, J. Harmand, B. Fimland, and H. Weman, "Wurtzite GaAs/AlGaAs Core-Shell Nanowires Grown by Molecular Beam Epitaxy," *Nanotechnology*, vol. 20, 2009.

[41] L. S. P. Frank L. Pedrotti, Leno M. Pedrotti, *Introduction To Optics*. Benjamin Cummings, 3 ed., 2006. 978-0131499331.

[42] T. Heinzel, *Mesoscopic Electronics in Solid State Nanostructures*. Wiley-VCH, 2007. 978-3-527-40638-8.